Chapter 2

Structure and Oxidation State of Silica-Supported Manganese Oxide Catalysts and Reactivity for Acetone Oxidation Using Ozone

2.1 Introduction

This chapter focuses on the characterization of silica-supported manganese oxide catalysts of different metal oxide loadings and the reactivity of these catalysts with respect to the acetone oxidation reaction using ozone. Raman spectroscopy measurements will be performed under reaction conditions to identify adsorbed intermediates on the catalyst surface. The catalysts with manganese oxide loadings of 3, 10, 15, and 20 wt. % will be characterized using x-ray absorption spectroscopy and x-ray diffraction (XRD). The reactivity of two of the silica-supported manganese oxide catalysts of different loading and structure will be measured for the acetone oxidation reaction using ozone and oxygen over the temperature range of 300 to 600 K. The main objective is to characterize the catalyst at different metal loadings and to relate the structure of the catalyst to its reactivity in the presence of oxygen or ozone.

2.2 Experimental Section

2.2.1 Materials

The manganese oxide catalysts were prepared using the incipient wetness impregnation method. Samples loaded with 3, 10, 15, and 20 wt. % of manganese oxide (using MnO_2 as the basis) were made using manganese acetate tetrahydrate ($Mn(CH_3COO)_2 \cdot 4H_2O$, Aldrich, 99.99 %) as the metal precursor. The support material, SiO_2 (Cabot, Cabosil EH-5), was calcined at 773 K for 6 h prior to impregnation. As an example, for the 10 wt. % sample 3.38 g (13.8 mmol) of manganese acetate tetrahydrate were dissolved in 25.5 cm^3 of distilled water, and this solution was then added dropwise to 10.8 g of SiO_2 while stirring. After impregnation, the sample was dried at 393 K for 6 h and then cooled and ground to ensure a homogeneous particle distribution. The sample was then heated to 773 K at a heating rate of 0.83 K/s (5 K/min) and was calcined at that temperature for 6 h.

Materials used in the XAFS experiments included Mn Powder (Alfa Aesar, 99.3 %), MnO (Cerac, 99.9 %), MnO_2 (Johnson Matthey Electronics, 99+ %), Mn_2O_3 (Cerac, 99.9 %), Mn_3O_4 (Johnson Matthey Electronics), and boron nitride (Aldrich, 99 %). The gases used in this study included oxygen (Air Products, > 99.6 %), hydrogen (Air Products, > 99.6 %), and helium (Air Products, > 99.6 %). They were passed through a gas purifier (Alltech, Model 4658) to eliminate moisture. Liquid acetone (Burdick and Jackson, 99.9+ %) was used in the Raman spectroscopy and reactivity experiments and was used as received.

2.2.2 Characterization

Temperature program reduction (TPR) measurements were performed on the 3, 10, 15, and 20 wt. % MnO_x/SiO_2 samples using a standard flow system equipped with a computer-interfaced mass spectrometer (Dycor / Ametek Model MA100) to monitor the H_2O^+ (*m/e* = 18) reduction signal [1]. Quantities of about 0.2 g of the samples were pretreated in oxygen at 773 K for 2 h at a flow rate of 53 μmol/s (77 cm^3/min) to remove excess moisture and carbonaceous impurities. The TPR measurements were carried out in pure hydrogen with a flow rate of 68 μmol/s (100 cm^3/min) and a heating rate of 0.03 K/s (2 K/min) from room temperature to 1073 K. The temperature at the onset of bulk reduction was defined as the reduction temperature (T_{red}) and was used for the pretreatment of samples prior to oxygen chemisorption determinations.

Oxygen chemisorption measurements were carried out in the same flow system used for the TPR experiments. Again, approximately 0.2 g of catalyst were pretreated in oxygen as for the TPR measurements and were then reduced in 68 μmol/s (100 cm^3/min) of hydrogen flow at the reduction temperature (T_{red} = 463 K) for 2 h. Following reduction, periodic pulses (19.6 μmol) of oxygen were introduced to the sample, and the oxygen uptake was measured by monitoring the O_2^+ signal (*m/e* = 32). The injection of oxygen to the sample was continued until equal oxygen peak areas were obtained to indicate surface saturation. The area under the oxygen peak at saturation was designated as A_{sat} and equaled 19.6 μmol. The total amount of adsorbed oxygen on the sample was estimated by the difference in area of the saturation peaks compared to the peaks obtained before saturation. The adsorbed oxygen combined with the mass of catalyst used in the

experiment allowed the determination of the metal dispersion of the samples. The exact equation used for determining the molecular oxygen uptake value was the following:

$$O_2\ Uptake\ (\mu mol\ g^{-1}) = \frac{5.59\,\mu mol}{m}\sum_i\left(\frac{A_{sat} - A_i}{A_{sat}}\right) \tag{2.1}$$

where m is the mass of the catalyst sample (g) and A_i is the measured area of an oxygen peak before saturation.

The specific surface area (SA) of each catalyst sample was obtained with an automated volumetric adsorption apparatus (Micromeritics, ASAP 2000) using a 6-point BET analysis. Approximately 0.2 g of catalyst were loaded into a quartz reactor, and the sample was degassed at 393 K in vacuum (< 670 mPa) prior to the measurements.

X-ray absorption fine structure (XAFS) measurements were carried out on the 3, 10, 15, and 20 wt. % MnO_x/SiO_2 samples. The samples were treated in a mixture of oxygen and helium flow (20% O_2) at 723 K for 3 h and were then transferred to glass cells with Kapton windows. The cells were sealed by glassblowing without exposure to the atmosphere. Along with the catalyst samples, reference samples were also analyzed including Mn, MnO, MnO_2, Mn_2O_3, and Mn_3O_4 all in fine powder form. For the reference compounds boron nitride powder was added to dilute the samples (90 % dilution by weight), which alone were too dense for XAFS analysis.

The XAFS measurements for the catalyst and reference samples were carried out in the X18B beamline in Brookhaven National Laboratory. The beamline was operated at close to 2.5 GeV with a 300-400 mA ring current, and the measurements were made in transmission mode with a Si(111) crystal monochromator, which resulted in an energy resolution of 2 eV. The k^3-weighted EXAFS spectra were Fourier transformed over k = 25-1400 nm^{-1}. Inverse Fourier transforms for each peak were analyzed using a curve

fitting method in the EXAFS analysis program WINXAS 2.03. The backscattering amplitude and phase shift functions for the Mn-O and Mn-Mn bonds were obtained from the model compound MnO_2. Simulated EXAFS spectra were generated using the computer program FEFF 8.2 [2].

X-ray Diffraction patterns were obtained with a diffractometer (Scintag ASC-0007) equipped with a Cu Kα radiation source (λ = 0.15418 nm, current = 40 mA, voltage = 45 kV). The 3, 10, 15, and 20 wt. % MnO_x/SiO_2 samples were scanned over a 2θ angle range of 10^o to 90^o at a rate of 1.5^o/min.

2.2.3 Spectroscopic and Reactivity Measurements

Laser Raman spectroscopy data were obtained in a system capable of simultaneous kinetic and spectroscopic measurements. The schematic is shown in Figure 2.1. The spectroscopic part of the system was made up of an argon ion laser (514.5 nm, Spex Lexel 95) as a light source, a holographic notch filter (Kaiser, Super Notch Plus) to reduce Rayleigh scattering, a single stage monochromator (Spex, 500 M) for the energy dispersion of the light, and a CCD detector (Spex, Spectrum One) for spectral acquisition. The detector slit width was set at 100 μm giving a resolution of 6 cm^{-1}. The laser was operated at around 160 mW giving a power at the sample of 140 mW.

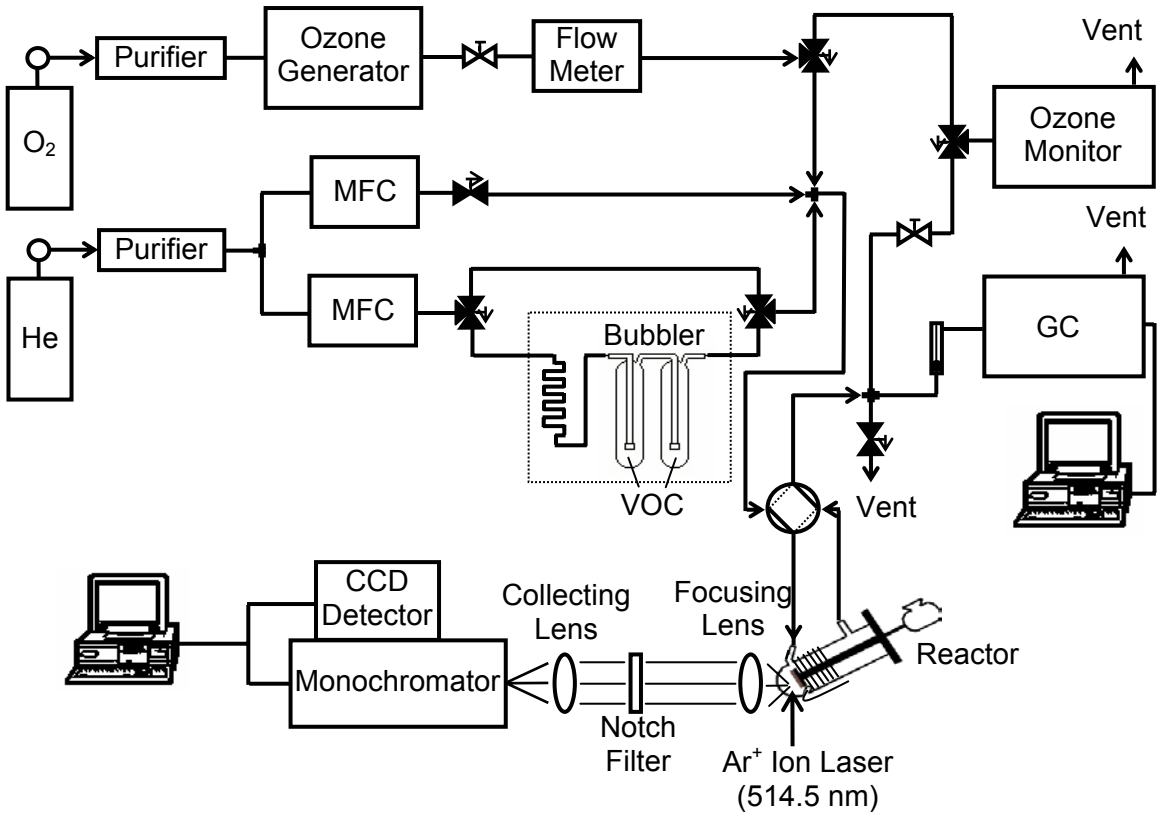

Figure 2.1. *In situ* Laser Raman spectroscopy system.

The catalyst sample was pressed into a thin wafer of 0.1 cm thickness and 1.5 cm diameter and was held in place by a stainless steel cap at the end of a ceramic rod. The rod was enclosed by a synthetic quartz (Suprasil) cell provided with heating tape and inlet and outlet ports, so as to serve as a reactor. The catalyst temperature was measured by a thermocouple that was placed in a well 3 mm from the sample.

The reactor part of the system was attached to the Raman spectrometer and included a gas delivery system equipped with a two-stage bubbler for the vaporization of liquid acetone. The bubbler was placed inside a refrigerated recirculator (Cole Parmer, Model 1268-14) and was maintained at a temperature of 273 K. The acetone vapor pressure (9.25 kPa) was calculated from the Antoine equation, $\log_{10} P_v = A - \frac{B}{T + C}$,

where P_v is the vapor pressure (mm Hg), T is the temperature (^oC), and the constants A, B, and C have values of 7.02447, 1161.0, and 224, respectively [3]. The flow from the bubbler was diluted to achieve the desired acetone concentration. Ozone was produced via corona discharge by passing pure oxygen through a high voltage ozone generator (OREC, V5-0), and its concentration was measured with an ozone monitor (In USA, Model H1). A gas chromatograph (GC) (SRI, Model 8610C) equipped with flame ionization and thermal conductivity detectors was used for measuring acetone, CO, and CO_2 concentrations. A Hayesep A 80/100 (Alltech, 6' × 1/8" × 0.085" SS) column was connected to the FID and was used for acetone while a 10.0 % AT-1000 80/100 CW-AW (Alltech, 36' × 1/8" × 0.086" AT-Steel) column was connected to the TCD and was used to separate CO and CO_2. The chromatograph was able to detect other possible reaction products, but none were detected.

Raman spectroscopy experiments were performed *in situ* on the 10 wt. % MnO_x/SiO_2 sample. The sample was pretreated at 723 K for 2 h in an oxygen and helium stream to remove excess moisture and carbonaceous impurities from the sample. The total flow rate of the feed was 340 μmol/s (500 cm^3/min) and was made up of 0.2 mol% (2,000 ppm) acetone, 1.0 mol % (10,000 ppm) ozone, 34 mol % oxygen, and helium as the balance. The total space velocity based on sample volume was 170,000 h^{-1}.

The reactivity studies employed the same experimental setup used for the laser Raman spectroscopy measurements. The flow conditions were also the same (2,000 ppm acetone and 10,000 ppm ozone) with the total flow rate equal to 340 μmol/s (500 cm^3/min). Catalyst activity was investigated as a function of temperature, and experiments were run on the 3 and 10 wt. % MnO_x/SiO_2 samples. A similar, blank

reactivity experiment was also conducted for the reaction between acetone and ozone with no catalyst or support present in the reactor.

2.3 Results and Discussion

2.3.1 TPR, Oxygen Chemisorption, Surface Area, and XRD Measurements

The TPR technique was used to find the reduction temperature, T_{red}, for the series of silica-supported manganese oxide catalysts. The reduction temperature was determined at the point where the H_2O^+ mass spectrometer signal (*m/e* = 18) increased dramatically and was taken to be the temperature right before the onset of bulk reduction, where principally the surface is expected to be reduced. Oxygen chemisorption experiments were then performed at the reduction temperature to determine the number of surface sites for the catalyst sample. Although giving just an estimate, this method gives a reasonable approximation of the number of surface sites, as will be seen from the comparison of the uptakes to the number of surface metal atoms as obtained from the x-ray line-broadening results.

Figure 2.2 shows the H_2O^+ (*m/e* = 18) TPR traces for the MnO_x/SiO_2 catalyst series. The TPR traces were normalized with respect to N_2 calibration peaks taken before and after the TPR experiment. The onset reduction temperature (T_{red} = 463 K) was the same for the four samples with different metal oxide loadings. Each trace shows a slight increase in signal at low temperature (< 373 K), which can be attributed to the initial stages of surface reduction. The traces show an initial bulk reduction peak of manganese oxide located at 543 K for all four samples and an additional reduction peak at around

644 K for the higher loading samples (10, 15, and 20 wt. % MnO_x/SiO_2). These two different and distinct reduction peaks were attributed to the sequential reduction of the manganese oxide phase as temperature was increased. The increase in signal above 800 K shown in the four catalyst samples was attributed to the dehydroxylation of the SiO_2 support [4].

The surface areas, molecular oxygen uptake values, and dispersions for the catalyst series are reported in Table 2.1. The surface area of the sample decreased with increasing manganese oxide loading, probably because the supported phase promoted sintering of the support by particle agglomeration. The oxygen uptake was the highest for the lowest loading sample, indicating high dispersion. The uptake was reduced and fairly constant for the higher loading samples probably because the lower surface area and increased crystallite size of these samples were compensated by the higher concentration of active phase.

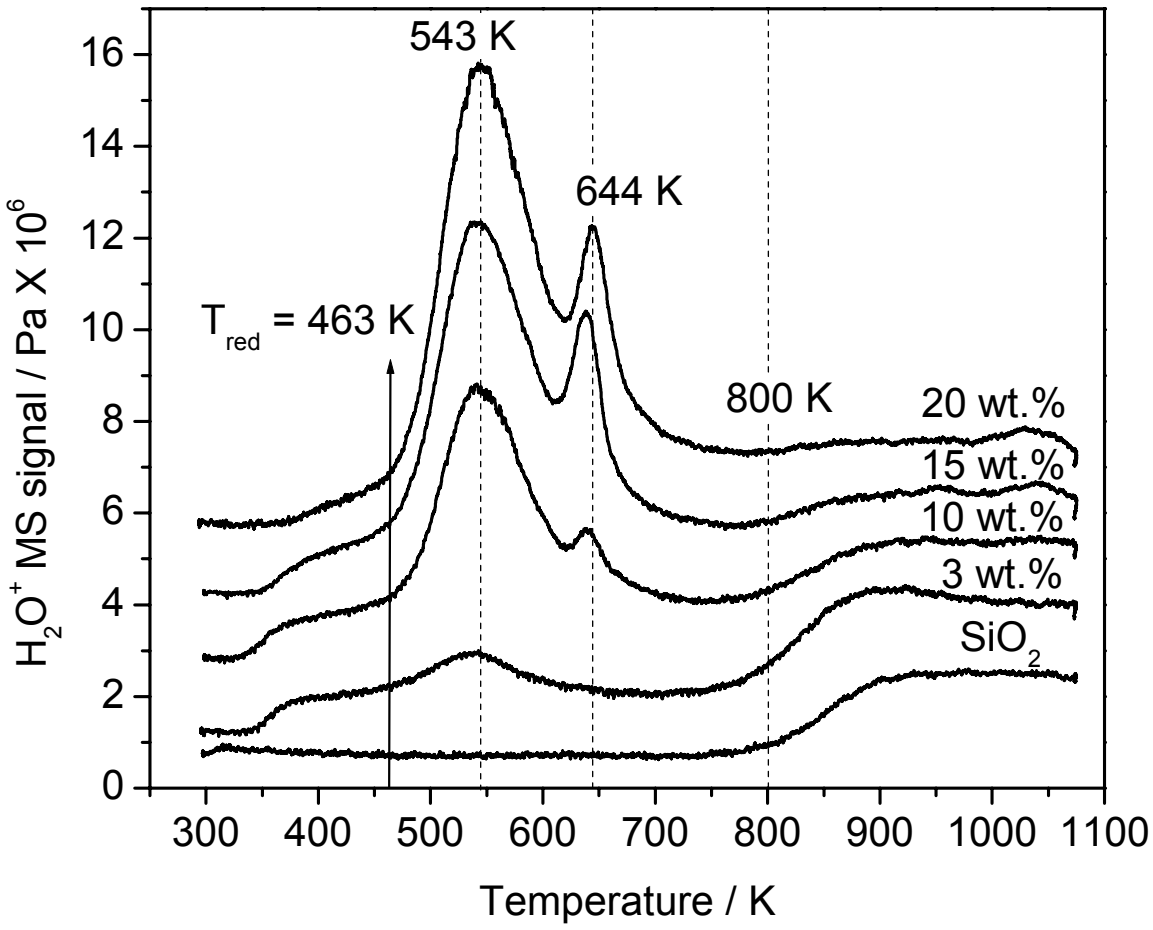

Figure 2.2. TPR traces for the MnO_x/SiO_2 catalytic series.

Table 2.1. Surface area, molecular oxygen chemisorption, and dispersion values for the catalyst series and pure silica.

Catalyst	SA m^2g^{-1}	O_2 Uptake $\mu molg^{-1}$	D_{chem} %
SiO_2	320	-	-
3 wt.% MnO_x/SiO_2	230	98	56
10 wt.% MnO_x/SiO_2	210	49	8.4
15 wt.% MnO_x/SiO_2	180	49	5.6
20 wt.% MnO_x/SiO_2	160	52	4.5

Oxygen chemisorption was used to estimate the number of reduced surface manganese atoms on the supported catalysts. Previous studies done on molybdenum oxide catalysts showed that this technique effectively measured the surface concentration of metal oxide species [1]. Oxygen chemisorption values are important in calculating turnover frequencies used in the reactivity analysis. Turnover frequency can be defined as the number of moles of reactant reacted per second per mole of exposed manganese atoms [5] and is obtained from the atomic oxygen uptake assuming one oxygen atom adsorbs per surface Mn atom. Thus, for turnover frequency calculations, the molecular oxygen uptake values (Table 2.1) were multiplied by 2. Turnover frequencies provide a useful means of comparing activity among catalysts of different metal loadings [6]. Dispersion is defined as the fraction of total manganese atoms at the surface of the catalyst. It is calculated by dividing the atomic oxygen uptake value by the total manganese atom loading, which can be determined from the catalyst preparation [7].

The x-ray diffraction results for the fresh 3, 10, 15, and 20 wt. % MnO_x/SiO_2 catalyst samples along with that of pure silica are shown in Figure 2.3. The large, broad peak located at $2\theta \sim 23^o$ is due to amorphous silica. The 3 wt. % silica-supported manganese oxide sample did not show any features corresponding to the metal oxides, and its XRD pattern resembled that of the pure silica support. This indicated that for the 3 wt. % MnO_x/SiO_2 catalyst, the manganese oxide was either well dispersed on the surface of the support or that the crystallized manganese oxide was not present in large enough quantities in the bulk to be detected through XRD.

For the 10, 15, and 20 wt. % manganese oxide samples, however, features were observed at $2\theta = 18.0^o$, 28.8^o, 32.3^o, and 36.1^o. Even though for the 10 wt. % MnO_x/SiO_2 sample these peaks were faint, they could be clearly discerned. The peaks were seen more distinct in the 15 and 20 wt. % MnO_x/SiO_2 samples. The features found in these diffractograms were compared to the lines of reference materials to determine what manganese oxide phases were present in these catalyst samples. The most intense lines for a Mn_3O_4 reference (PDF # 800382), shown in the bottom of Figure 2.3, matched the features found in the 15 and 20 wt. % MnO_x/SiO_2 catalyst samples.

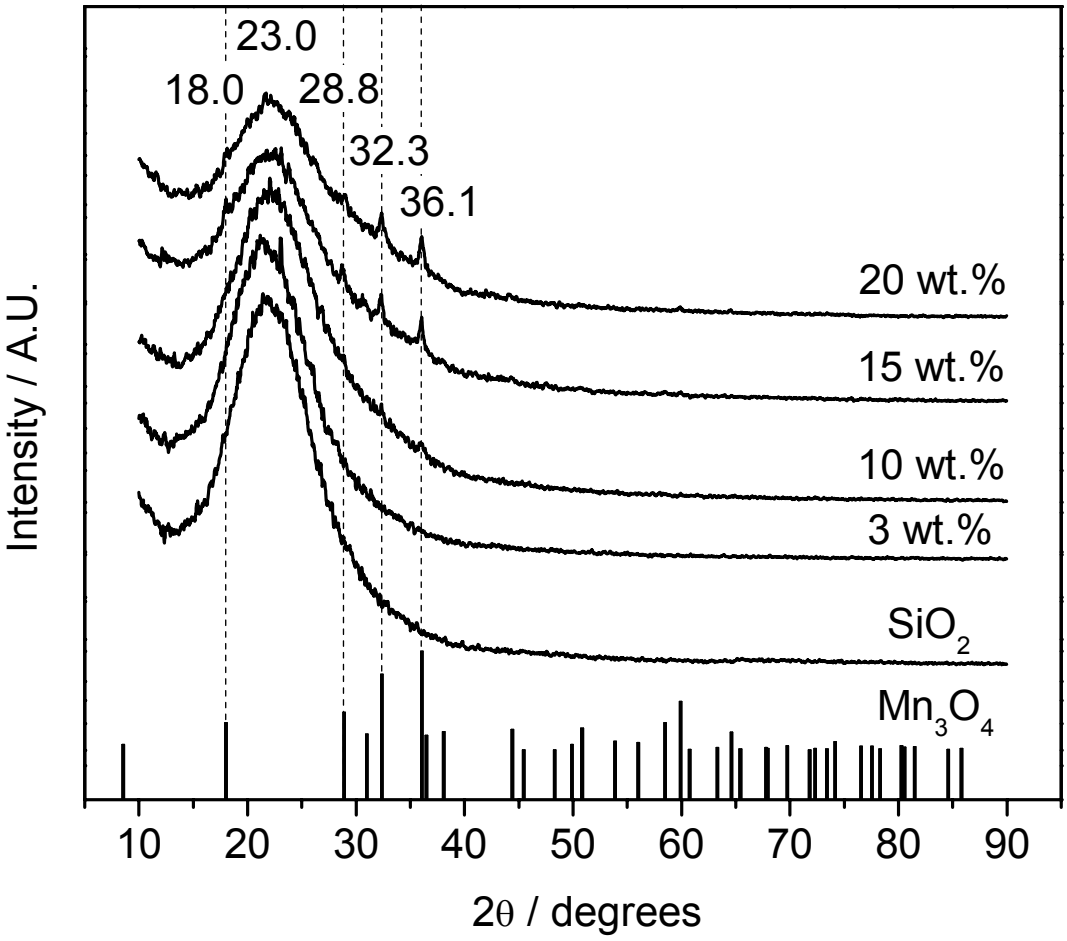

Figure 2.3. XRD results for the MnO_x/SiO_2 catalytic series along with reference lines for Mn_3O_4.

The manganese oxide crystallite sizes for the 15 and 20 wt. % catalyst samples were estimated by x-ray line-broadening analysis, and the results are shown in Table 2.2. The particle sizes were calculated using the Sherrer formula, $d = \frac{K\lambda}{\beta\cos\theta}$, where d is the particle diameter (nm), K is a constant taken to be 0.9, λ is the x-ray wavelength (nm), β is the FWHM of the diffraction peak (radians) corrected for instrumental broadening (0.1^o), and θ is the diffraction angle [8]. The two strongest diffractions lines at 2θ of

32.3° (103) and 36.1° (211) were chosen for analysis. The average crystallite size was 21 nm for both the 15 and 20 wt. % MnO_x/SiO_2 catalyst samples. Using the crystal structure for Mn_3O_4 [9] (Fig. 2.4) and its corresponding lattice parameters (a = 0.5769 nm, b = 0.5769 nm, c = 0.9460 nm), it was determined that there are 4, 2, and 2 atoms on the ac, ab, and bc unit cell faces, respectively. From this information, an average surface Mn atom density of 5.66×10^{18} m^{-2} was calculated. Thus, a 21-nm cubic crystallite will contain roughly 15,000 surface Mn atoms. Taking the density of Mn_3O_4 to be 4.856 g/cm^3, and considering the crystallite size was calculated to be the same for both the 15 and 20 wt. % MnO_x/SiO_2 catalyst samples, the dispersion can be calculated to be 4.2 % for both samples. This value is in reasonable correspondence to the dispersion values calculated from the atomic oxygen uptake experiments with dispersions of 5.6 % and 4.5 % for the 15 and 20 wt. % catalyst samples, respectively. Thus, it can be concluded that the oxygen chemisorption experiments give a fair estimate of the number of surface manganese sites.

Table 2.2. X-ray diffraction data, particle size, and dispersion values for the 10 and 15 wt. % MnO_x/SiO_2 catalysts.

Sample	2θ / °	β / °	d / nm	D_{XRD} / %
15 wt.% MnO_x/SiO_2	32.3 36.1	0.38 0.42	~21	4.2
20 wt.% MnO_x/SiO_2	32.3 36.1	0.36 0.46	~21	4.2

2.3.2 X-ray Absorption Fine Structure (XAFS)

Figures 2.4, 2.5, and 2.6 show the crystal structures and corresponding unit cells for Mn_3O_4 [9], β-Mn_2O_3 [10], and β-MnO_2 [11]. Table 2.3 presents the coordination and bond lengths for the same three structures [9,10,11]. The crystal structure of Mn_3O_4 (Fig. 2.4) is that of a distorted spinel with a tetragonal lattice containing two types of Mn atoms of different Mn-O coordination. The first type of Mn atom, referred to in Figure 2.4 as Site 1, has a Mn-O coordination number of 6 while the second Mn atom type, referred to as Site 2, has a Mn-O coordination number of 4. The first Mn site has 4 Mn-O bonds of length 0.1932 nm, 2 Mn-O bonds of length 0.2284 nm, and 2 Mn-Mn bonds of length 0.2884 nm, while the second Mn site has 4 Mn-O bonds of length 0.2044 nm. The crystal structure of β-Mn_2O_3 (Fig. 2.5) is that of bixbyite with a cubic lattice also containing two types of Mn atoms each having a Mn-O coordination number of 6. The first type of Mn atom, referred to in Figure 2.5 as Site 1, has 6 Mn-O bonds of length 0.1993 nm while the second type of Mn atom, referred to as Site 2, has 2 Mn-O bonds of length 0.1899 nm, 2 Mn-O bonds of length 0.1984, and 2 Mn-O bonds of length 0.2248 nm. There are no Mn-Mn bonds for either site that are less than 0.3 nm in length. The crystal structure of β-MnO_2 (Fig. 2.6) is that of rutile with a body-centered tetragonal lattice and a Mn-O coordination number of 6. The structure has 2 Mn-O bonds of length 0.1877 nm, 4 Mn-O bonds of length 0.1891 nm, and 2 Mn-Mn bonds of length 0.2871 nm. Figure 2.7 shows the results of an analysis with FEFF 8.2 [2] that gives the simulated EXAFS spectrum for β-MnO_2, the two simulated spectra for the two Mn sites of β-Mn_2O_3, and the two simulated spectra for the two Mn sites in Mn_3O_4. The types of

bonding associated with each feature are also shown for the four simulated EXAFS spectra.

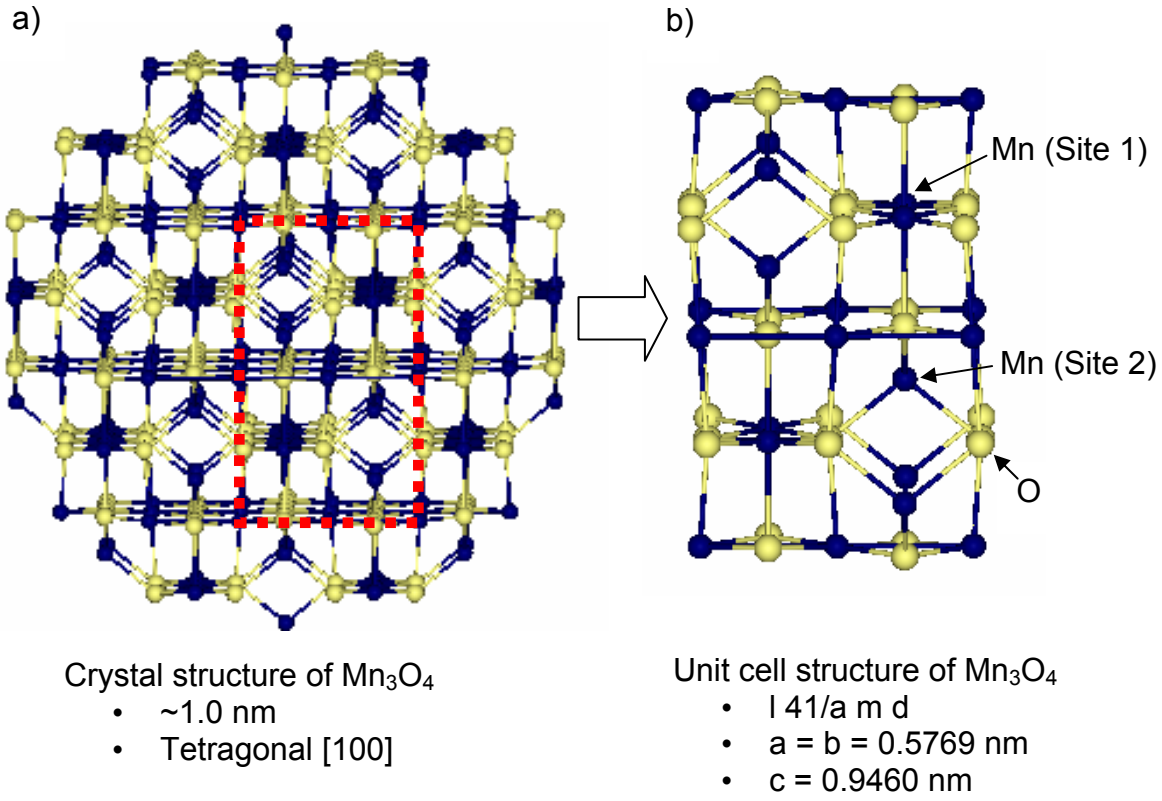

Figure 2.4. Crystal structure and unit cell for Mn_3O_4.

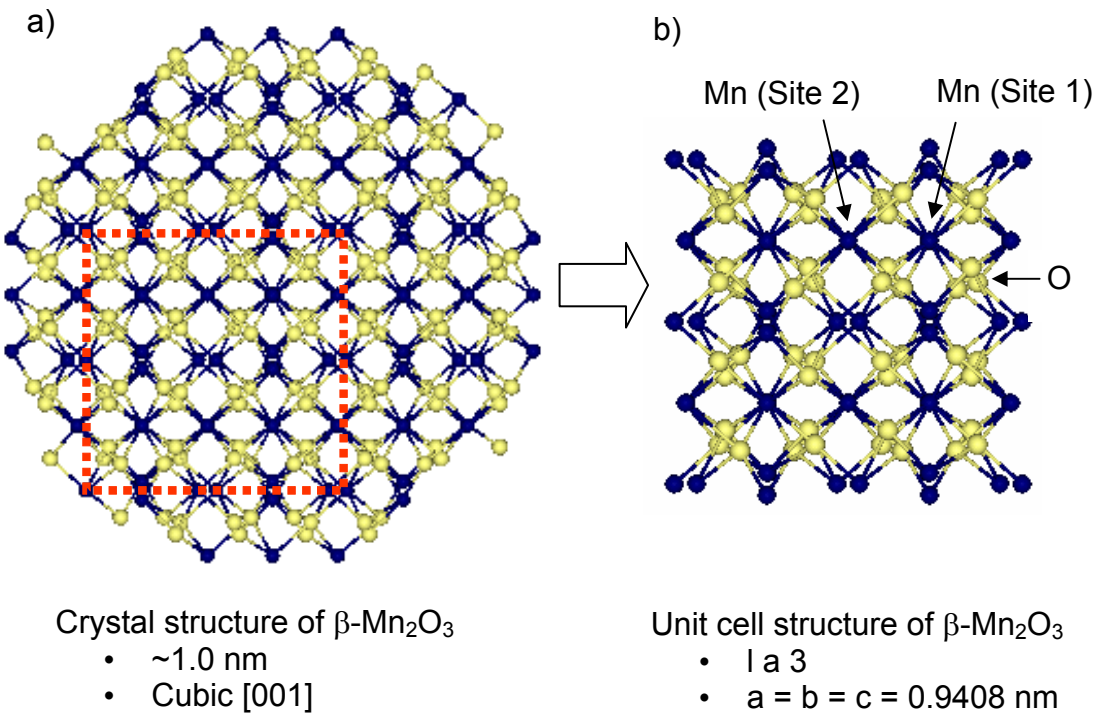

Figure 2.5. Crystal structure and unit cell for β-Mn_2O_3.

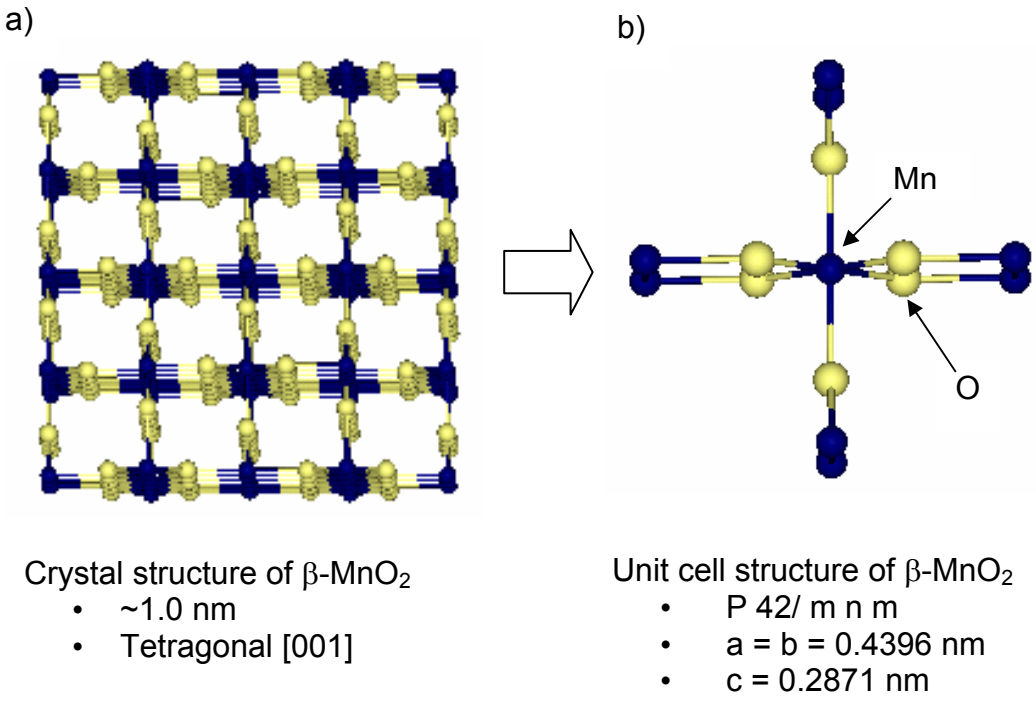

Figure 2.6. Crystal structure and unit cell for β-MnO_2.

Table 2.3. Coordination numbers and bond lengths for the crystal structures of β-MnO_2, β-Mn_20_3, and Mn_3O_4.

MnO_2			Mn_2O_3					Mn_3O_4				
				Mn (Site 1)		Mn (Site 2)			Mn (Site 1)		Mn (Site 2)	
Bonding	CN	D / nm	Bonding	CN	D / nm	CN	D / nm	Bonding	CN	D / nm	CN	D / nm
Mn-O	2	0.1877	Mn-O	6	0.1993	2	0.1899	Mn-O	4	0.1932	4	0.2044
	4	0.1891				2	0.1984		2	0.2284		
						2	0.2248					
Mn-Mn	2	0.2871						Mn-Mn	2	0.2884	8	0.3435
			Mn-Mn	6	0.3104	2	0.3104		4	0.3123		
Mn-O	4	0.3343		6	0.3564	4	0.3121		4	0.3435		
						2	0.3564					
Mn-Mn	8	0.3424				4	0.3579	Mn-O	2	0.3552	8	0.3477
			Mn-O	6	0.3618				4	0.3789		
Mn-O	4	0.3430		6	0.3843	2	0.3680		2	0.3802		
	8	0.3905				2	0.3697					
						2	0.3728	Mn-Mn	2	0.3829	4	0.3730
						2	0.3789				4	0.3829
						2	0.3958					
						2	0.4097	Mn-O			4	0.3854

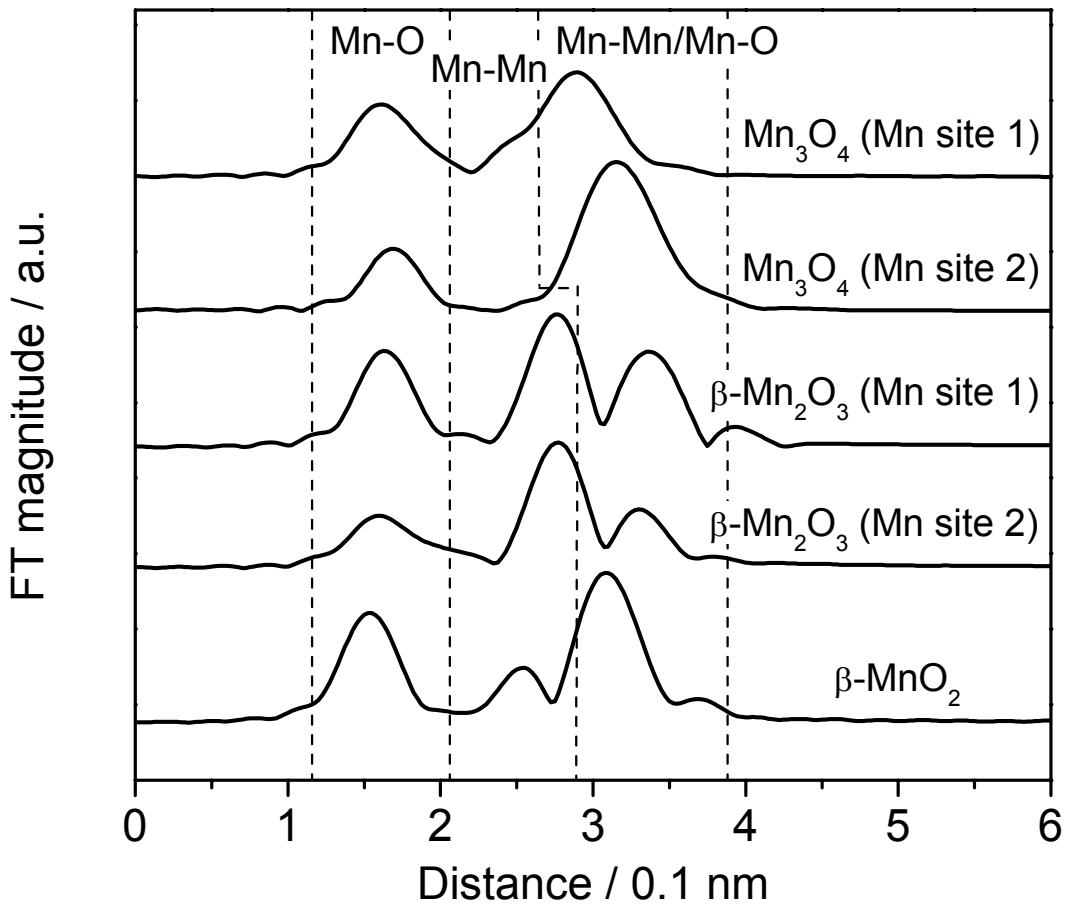

Figure 2.7. Simulated EXAFS spectra for β-MnO_2, β-Mn_2O_3, and Mn_3O_4 using FEFF 8.2.

Figure 2.8a) shows the k^3-weighted extended x-ray absorption fine structure (EXAFS) oscillations for the 3 wt. % MnO_x/SiO_2, 10 wt. % MnO_x/SiO_2, 15 wt. % MnO_x/SiO_2, 20 wt. % MnO_x/SiO_2, MnO, Mn_3O_4, Mn_2O_3, and MnO_2 samples while Figure 2.8b) shows their corresponding Fourier transforms. The MnO reference spectrum (Fig. 2.8b)) gave two main peaks at 0.178 and 0.273 nm. The first peak was assigned to Mn-O bonds while the large, second feature was most likely due to a mixture of Mn-O and Mn-Mn bonds. For the Mn_3O_4 reference spectrum (Fig. 2.8b)), two strong

peaks at 0.152 and 0.300 nm were assigned to Mn-O bonds and a mixture of both Mn-O and Mn-Mn bonds, respectively. A small peak also appeared at 0.236 nm, which was due to Mn-Mn bonding. These bonding assignments are confirmed by the simulated EXAFS spectra done for Mn_3O_4 shown in Figure 2.7. The Mn_2O_3 reference spectrum (Fig. 2.8b)) resulted in two main peaks located at 0.148 and 0.273 nm. The first peak was again assigned to Mn-O bonding while the larger second peak was most likely due to Mn-Mn bonding according to the two simulated spectra for Mn_2O_3 shown in Figure 2.7. For the MnO_2 reference spectrum (Fig. 2.8b)), a strong peak appeared at 0.151 nm, which was assigned to a Mn-O bond while peaks at 0.250 and 0.309 nm were assigned to Mn-Mn bonds and a mixture of Mn-O and Mn-Mn bonds in the second and third shells, respectively. Again, these bonding assignments are confirmed by the simulated EXAFS spectra for β-MnO_2 shown in Figure 2.7.

For the SiO_2 supported samples a strong peak at 0.147 nm appeared, which was assigned to Mn-O bonding. Peaks with very weak intensity also appeared at 0.238 and 0.284 nm in the second and third shells. The lack of peak intensity for the higher shells was probably a result of a combination of factors. First, the small size of the MnO_x crystallites due to the limited loading on the support, and second, the use of room temperature in the measurement of the x-ray absorption spectra, which resulted in thermal broadening of the signal from the higher shells. The observation of XRD diffraction lines for Mn_3O_4 indicates that there are a few large crystallites, but the low Mn-Mn coordination suggests the presence of smaller units. Thus, the sample is heterogeneous with a range of supported structures.

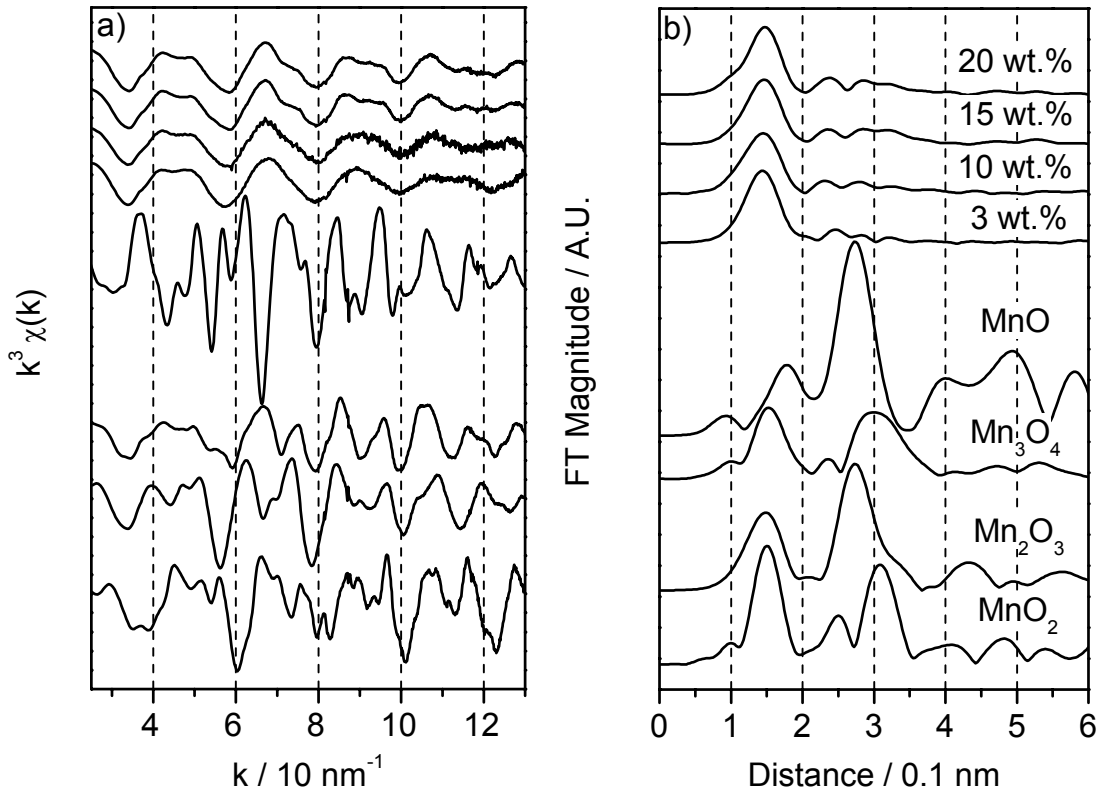

Figure 2.8. Mn K-edge EXAFS spectra for the MnO_x/SiO_2 catalytic series and the reference compounds MnO, Mn_3O_4, Mn_2O_3, and MnO_2 a) in k^3-weighted space and b) the corresponding Fourier transforms.

Results from the quantitative analysis done on the EXAFS data are summarized in Table 2.4. Shown in the table are the Mn-O and Mn-Mn coordination numbers, CN, and bond distances, R, for the supported catalyst samples. Also given in the table are values for the Debye-Waller factor (σ^2), energy shift (ΔE), and residual factor (R_f), which describes the quality of the fit. R_f is defined as

$$R_f = \left(\frac{\sum_{i=1}^{N} \left| y_{\exp}(i) - y_{theo}(i) \right|}{\sum_{i=1}^{N} y_{\exp}(i)} \right) \times 100 \qquad (2.2)$$

where y_{exp} and y_{theo} are the experimental and theoretical data points, respectively.

It is known from the crystal structures [9,10,11] shown in Figures 2.4, 2.5, and 2.6 that for β-MnO_2 and β-Mn_2O_3 the Mn-O coordination numbers are both 6 while for Mn_3O_4 the Mn-O coordination is 6 for one site and 4 for the other. For the supported samples the Mn-O coordination number decreased with increasing metal oxide loading with a range of coordination number values between 5 and 6 (Table 2.4). For example, the Mn-O coordination number for the 3 wt. % MnO_x/SiO_2 was 6.02 and, therefore, resembled that of β-MnO_2 or β-Mn_2O_3, while that of the 20 wt. % MnO_x/SiO_2, decreased to 5.05, a value that is similar to the average Mn-O coordination number for Mn_3O_4. The Mn-O bond distance, R, also showed a trend, increasing with higher loading. This trend was associated with a decrease in the strength of the Mn-O bond as the Mn-O coordination number and oxidation state decreased.

The Mn-Mn coordination number increased with increased metal oxide loading. The coordination numbers were small and all under one and indicated little Mn-Mn bonding and only the beginning stages of crystallite formation. However, this increase did give insight about the manganese oxide structure of the catalyst samples. For the 3 wt. % MnO_x/SiO_2 sample, the Mn-Mn coordination number was 0.017 which suggested that there was essentially no Mn-Mn bonding, and the sample had an atomically dispersed manganese oxide phase. At higher manganese oxide loadings, the Mn-Mn coordination number increased slightly approaching a value close to one.

Table 2.4. EXAFS curve-fitting results for MnO_x/SiO_2 catalyst series.

Catalyst	Mn-O					Mn-Mn				
	CN	R / nm	σ^2 / 10^{-5} nm^2	ΔE / eV	R_f / %	CN	R / nm	σ^2 / 10^{-5} nm^2	ΔE / eV	R_f / %
3 wt.% MnO_x/SiO_2	6.02	0.1885	5.195	-12.63	3.99	0.017	0.2873	0.512	-9.108	4.02
10 wt.% MnO_x/SiO_2	5.50	0.1898	2.986	-12.14	3.31	0.705	0.2786	0.655	-12.93	3.59
15 wt.% MnO_x/SiO_2	5.40	0.1908	2.726	-11.6	3.45	0.928	0.2809	0.770	-10.83	3.66
20 wt.% MnO_x/SiO_2	5.05	0.1919	1.742	-10.22	2.45	0.953	0.2817	0.659	-10.32	2.33

Overall, the results of the XAS characterization studies suggest a progression of structure with loading as indicated in Figure 2.9. At the lowest loading, the manganese center is isolated and 6-coordinate (Fig. 2.9a)). As the loading grows to the range of 10 wt. %, small MnO_x clusters are likely to be formed. These clusters (Fig. 2.9b)) may have a structure that is close to a building block of the Mn_3O_4 structure. The unit shown has two edge-sharing Mn-O octahedra and an attached Mn-O tetrahedron. This unit is actually a part of the Mn_3O_4 structure and contains the ratio of octrahedra/tetrahedra found in the bulk structure of 2 to 1 (Fig. 2.4). The closest Mn-Mn distance is between the octahedra, as the tetrahedral unit is bonded through a corner atom. The average Mn coordination is $[(2\times6)+(1\times4)]/3 = 5^1/_3$.

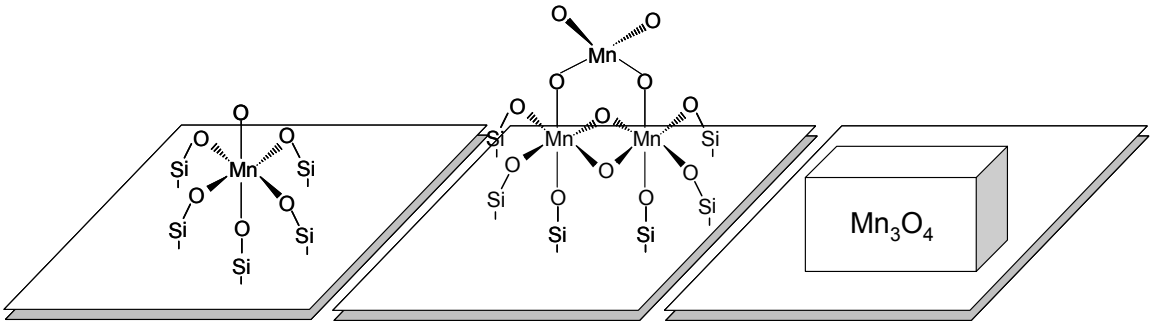

Figure 2.9. Manganese oxide clusters formed with increased loading from a) 3 wt. % MnO_x/SiO_2 to b) 10 wt. % MnO_x/SiO_2, and c) 15 and 20 wt. % MnO_x/SiO_2.

Figure 2.10a) presents the Mn K-edge x-ray absorption near-edge spectroscopy (XANES) spectra along with the characteristic energy for absorption, E_0, for the four silica-supported manganese oxide catalysts and the bulk MnO, Mn_3O_4, Mn_2O_3, and MnO_2 references. The absorption energies for the supported catalysts decreased with increasing

loading (6.5478 – 6.5472 eV) and fell between the energies obtained for Mn_2O_3 (6.5479 eV) and Mn_3O_4 (6.5467 eV). This gave evidence that the active manganese oxide phase for the supported samples was between the oxidation states of Mn_2O_3 (+3) and Mn_3O_4 (+2⅔). The values showed that at lower loadings, the oxidation state resembled that of Mn_2O_3 while at higher loadings, the oxidation state approached that of Mn_3O_4.

Relating this trend for absorption energies to the Mn-O bond distances found in Table 2.3, it can be inferred that as bond length increased, the energy for the absorption edge decreased. This same trend was seen in a study that also used EXAFS analysis to study silica-supported manganese oxides [12]. This broad study, which examined oxidation states ranging from metallic manganese to the permanganate ion, reported Mn-O bond distances decreasing from 0.283 to 0.170 nm and K-edge shifts increasing from 6.5380 to 6.5571 keV in moving from α-Mn to $KMnO_4$. Even though the results from the present study were narrower in scope, the Mn-O bond distances and edge positions (Table 2.3) were very similar to the values of 0.189 nm and 6.5531 keV reported for the silica-supported manganese oxide used in the previous study.

Figure 2.10b) shows the white line area analysis on the Mn K-edge XANES spectra for the silica-supported manganese oxide catalysts of different loadings. The analysis for determining the white line area began with fitting an arctangent function to the XANES spectrum. The curve from the arctangent fit was then subtracted from the original XANES data to generate a spectrum without the edge jump information. Finally, the resulting spectrum was fit to a Gaussian to determine the area of the white line. All four spectra, as well as the white line area calculated for each catalyst, are shown in Figure 2.10b). The white line areas for the supported catalysts decreased with increasing

metal oxide loading. The white line area is directly related to the transition of a 1s core electron to a bound state such as an empty or partially filled molecular orbital [13]. An increase in white line area corresponds to an increase in the density of empty states capable of accepting an electron. Thus, as the white line area decreases, the oxidation state of the Mn also decreases. This analysis further confirms that the 3 wt. % MnO_x/SiO_2 catalyst is in a higher oxidation state, such as MnO_2 (+4) or Mn_2O_3 (+3), than the oxidation state of the 10, 15, and 20 wt. % MnO_x/SiO_2 catalysts, which is most likely Mn_3O_4 (+2⅔).

Qualitative comparison of the XANES spectra in the white line region at 6.55 keV shows that the supported catalysts mostly resembled Mn_3O_4. Also, the fine structure for the silica-supported manganese oxides after the white line region was also very similar to that for Mn_3O_4. Therefore, based on the XAFS analysis, the dispersed manganese oxide phase for the silica-supported catalyst is deduced to be built from building blocks similar to those found in Mn_3O_4 as shown in Figure 2.9. The XRD patterns confirm this for the higher loading samples.

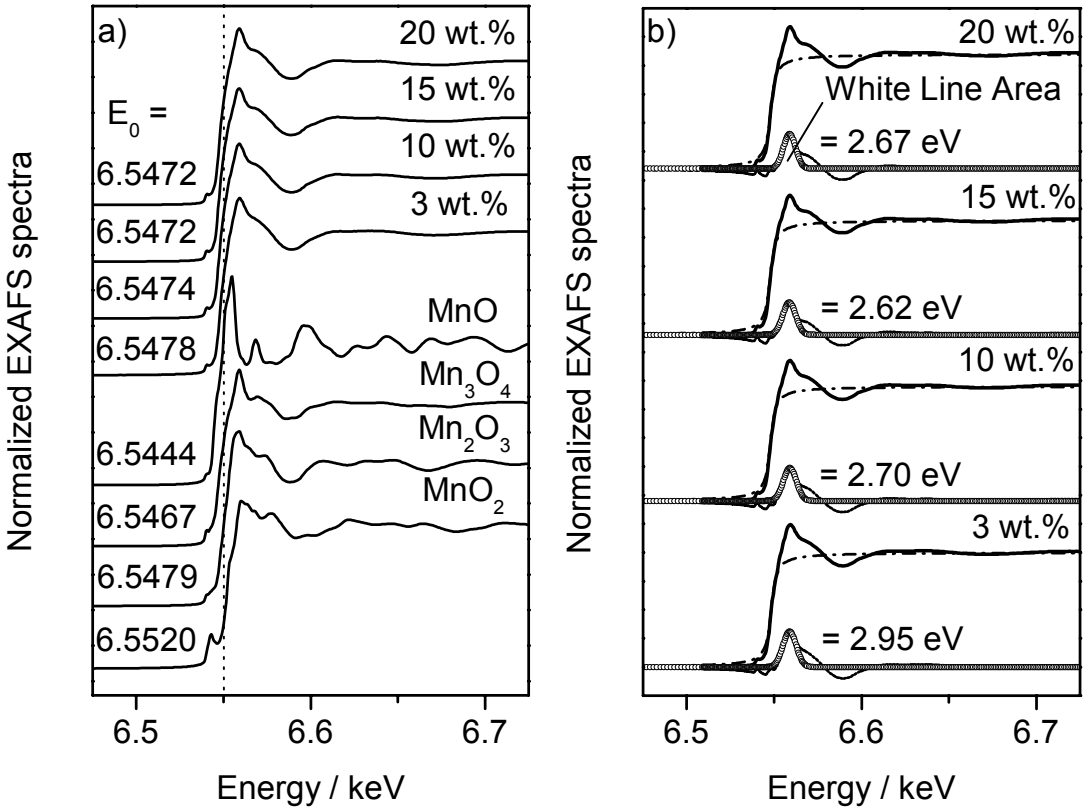

Figure 2.10. a) Mn K-edge XANES spectra and E_0 values for the MnO_x/SiO_2 catalytic series and the reference compounds MnO, Mn_3O_4, Mn_2O_3, and MnO_2 and b) white line area analysis on the Mn K-edge XANES spectra for the MnO_x/SiO_2 catalytic series.

2.3.3 Reactivity Studies

Reactivity studies as a function of temperature were performed on the 3 wt. % and 10 wt. % catalyst samples because the manganese phase in these samples was highly dispersed and had significant differences in structure. Turnover frequencies (TOFs) were calculated for both acetone and ozone using the atomic oxygen uptake values from the oxygen chemisorption experiments and the respective conversion values.

Figure 2.11 shows the rise of acetone conversion (Fig. 2.11a)) and TOF (Fig. 2.11b)) with temperature for the range of 300 to 600 K (0.2 mol % acetone, 1 mol % O_3, 34 mol % O_2). Comparison of the acetone conversion with ozone and oxygen as the oxidants shows a clear enhancement of the oxidation reaction by the ozone. On both the 3 wt. % MnO_x/SiO_2 and 10 wt. % MnO_x/SiO_2 catalysts the acetone conversion occurs 150 – 200 K lower with ozone. The catalysts had a greater effect on acetone conversion with ozone at low temperatures (T < 425 K), but showed little difference with the blank above 500 K. Both catalysts gave similar conversions below 400 K, but above this temperature the 10 wt. % MnO_x/SiO_2 catalyst yielded consistently higher acetone conversions. When ozone was not present in the acetone oxidation reaction, there was very little difference in acetone conversion for the 3 wt. % catalyst and 10 wt. % catalyst except at the highest temperature.

Conversion alone is not a good measure of catalytic activity when comparing catalysts of different loadings. In order to obtain a useful comparison, the activity should be expressed on the basis of surface metal atoms, and thus, turnover frequencies should be used. It is clear from Figure 2.11b) that the 10 wt. % MnO_x/SiO_2 catalyst was more active than the 3 wt. % MnO_x/SiO_2 catalyst for reactions with or without ozone. It also can be seen that ozone substantially increased the acetone oxidation TOF. For example, the acetone TOF found in the presence of ozone at 303 K was larger than the acetone TOF found in the absence of ozone at 500 K. The addition of ozone significantly reduced the temperature at which acetone was oxidized. For both ozone and oxygen the reactivity increased slowly at low temperatures, and then more rapidly at high temperatures.

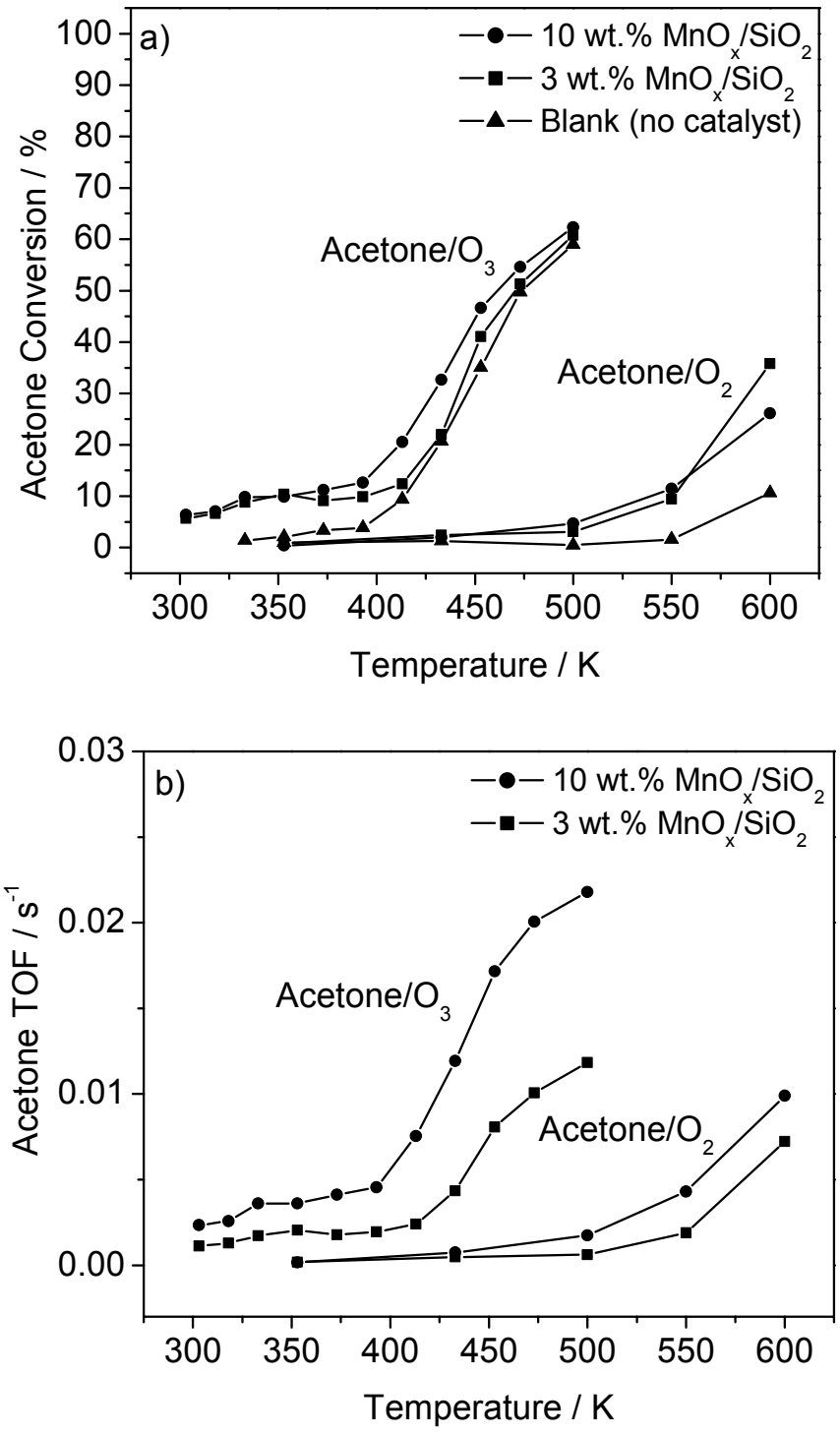

Figure 2.11. Acetone a) conversion and b) TOF versus temperature for 3 and 10 wt. % MnO_x/SiO_2 in the presence and absence of ozone (0.2 mol % acetone, 1 mol % O_3, 34 mol % O_2, 64.8 mol % He).

When ozone was included in the reacting mixture, the only observed product when using the 10 wt. % MnO_x/SiO_2 catalyst for temperatures less than 400 K was CO_2. For temperatures in the range of 400 – 450 K, CO was also produced with selectivities for CO_2 and CO being about 75 and 25 %, respectively. Above 450 K, the selectivities for CO_2 and CO were roughly 60 and 40 %, respectively. For the case when there was no ozone in the reacting mixture, the only observed product at all temperatures was CO_2.

Figure 2.12 shows the effect of temperature on ozone conversion and TOF at the same conditions as in Figure 2.11 for the 3 wt. % MnO_x/SiO_2, 10 wt. % MnO_x/SiO_2, and a blank. Data are presented for reactions between ozone and acetone and ozone alone (i.e. ozone decomposition). At low temperatures ($T < 425$ K) ozone conversion was greater when acetone was not included in the reaction.

Again, the activity of the 10 wt. % MnO_x/SiO_2 was higher than that of the 3 wt. % MnO_x/SiO_2 catalyst for reactions with or without acetone (Fig. 2.12b)). Greater ozone TOFs were observed in the reaction of pure ozone compared to the reaction with acetone for temperatures lower than 420 K for the 10 wt. % MnO_x/SiO_2 catalyst and lower than 460 K for the 3 wt. % MnO_x/SiO_2 catalyst. This behavior was most likely due to adsorbed acetone blocking the active sites used for the ozone reaction. Above 475 K the calculated ozone TOFs were similar in value regardless of whether acetone was included in the reacting mixture. This was due to the gas-phase thermal decomposition of ozone at these higher temperatures, which makes the rate of ozone decomposition independent of the reaction with acetone.

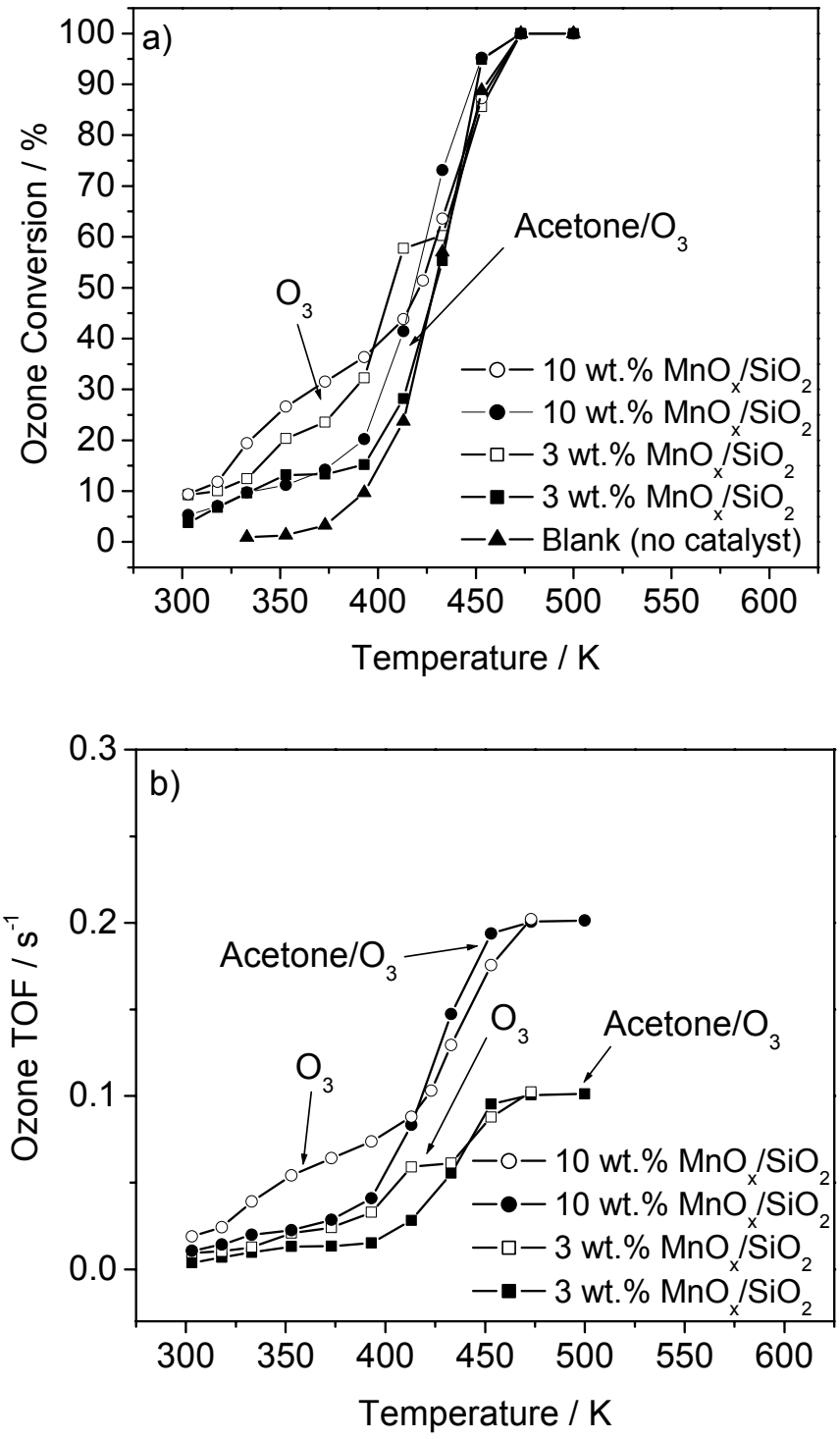

Figure 2.12. Ozone a) conversion and b) TOF versus temperature for 3 and 10 wt. % MnO_x/SiO_2 in the presence and absence of acetone (0.2 mol % acetone, 1 mol % O_3, 34 mol % O_2, 64.8 mol % He).

Activation energies of acetone conversion for both catalysts were determined from Arrhenius plots of the turnover frequencies. Figure 2.13a) presents Arrhenius plots for acetone conversion for the 3 wt. % MnO_x/SiO_2 catalyst for reactions with and without ozone. For the case when ozone was present, two regions were identified. In the high temperature region ($T > 400$ K, $T^{-1} < 2.5 \times 10^{-3}$ K^{-1}) when the ozone was mainly decomposed thermally, the activation energy was 35 kJ/mol. In the lower temperature region ($T < 400$ K) when the reaction took place on the surface of the catalyst, the activation energy was only 6.1 kJ/mol. For the case when ozone was not present, the reaction occurred at higher temperatures ($T > 500$ K, $T^{-1} < 2.0 \times 10^{-3}$ K^{-1}) with an activation energy of 34 kJ/mol. Figure 2.13b) presents the analogous plot for the 10 wt. % catalyst in reactions with and without ozone. When ozone was used, the activation energy was 30 kJ/mol in the upper temperature region ($T > 400$ K) and 7.3 kJ/mol in the lower region ($T < 400$ K). When ozone was not used, the activation energy was 33 kJ/mol at high temperatures ($T > 500$ K).

The analogous Arrhenius plots for ozone conversion for the 3 and 10 wt. % MnO_x/SiO_2 catalysts in the presence and absence of acetone are shown in Figure 2.14. Again, two temperature regions seemed to exist due to the thermal decomposition of ozone at higher temperatures. In the lower temperature region ($T < 400$ K) when acetone and ozone were competing for sites on the catalyst surface, the ozone TOF was depressed compared to the TOF for ozone alone. However, at higher temperatures ($T > 400$ K) when ozone decomposed thermally, the rate of ozone conversion increased dramatically. In the presence of acetone for the 3 wt. % MnO_x/SiO_2 sample in the upper temperature region ($T > 400$ K, $T^{-1} < 2.5 \times 10^{-3}$ K^{-1}), the activation energy was 46 kJ/mol while in the

lower temperature region (T < 400 K) the activation was found to be 15 kJ/mol. For the case when acetone was not included in the reacting mixture, the corresponding activation energy was18 kJ/mol. For the 10 wt. % MnO_x/SiO_2 (Fig. 2.14b)) catalyst when acetone was used, the activation energy was 39 kJ/mol in the upper temperature region (T > 400 K) and was 14 kJ/mol in the lower temperature region (T < 400 K). In the absence of acetone, the corresponding activation energy was 16 kJ/mol.

It is interesting that the rate for the acetone reaction accelerated in the temperature range of 400 – 500 K when most of the ozone was decomposed. This was likely due to the involvement of homogeneous free-radical reactions initiated from ozone derived precursors. The finding of two reaction regions has been reported in other oxidation reactions with ozone. In one study [14], two temperature regions were also observed for the oxidation of ethanol with ozone. When an alumina-supported manganese oxide catalyst was used for the ozone oxidation of ethanol, an activation energy of 48 kJ/mol was observed in the upper temperature region (T > 400 K) while an activation energy of 3.7 kJ/mol was observed in the low region (T < 400 K). When ozone was not present in the reaction, the activation energy was 89 kJ/mol in the temperature range of 416 – 526 K. When a silica-supported molybdenum oxide was used as the catalyst in the reaction between ethanol and ozone, two temperature regions were again observed. The activation energy was 70 kJ/mol in the upper temperature region (T > 523 K) and 10.0 kJ/mol in the lower region (T < 523 K). When ozone was not used, the activation energy was 92 kJ/mol over a temperature range of 475 – 555 K.

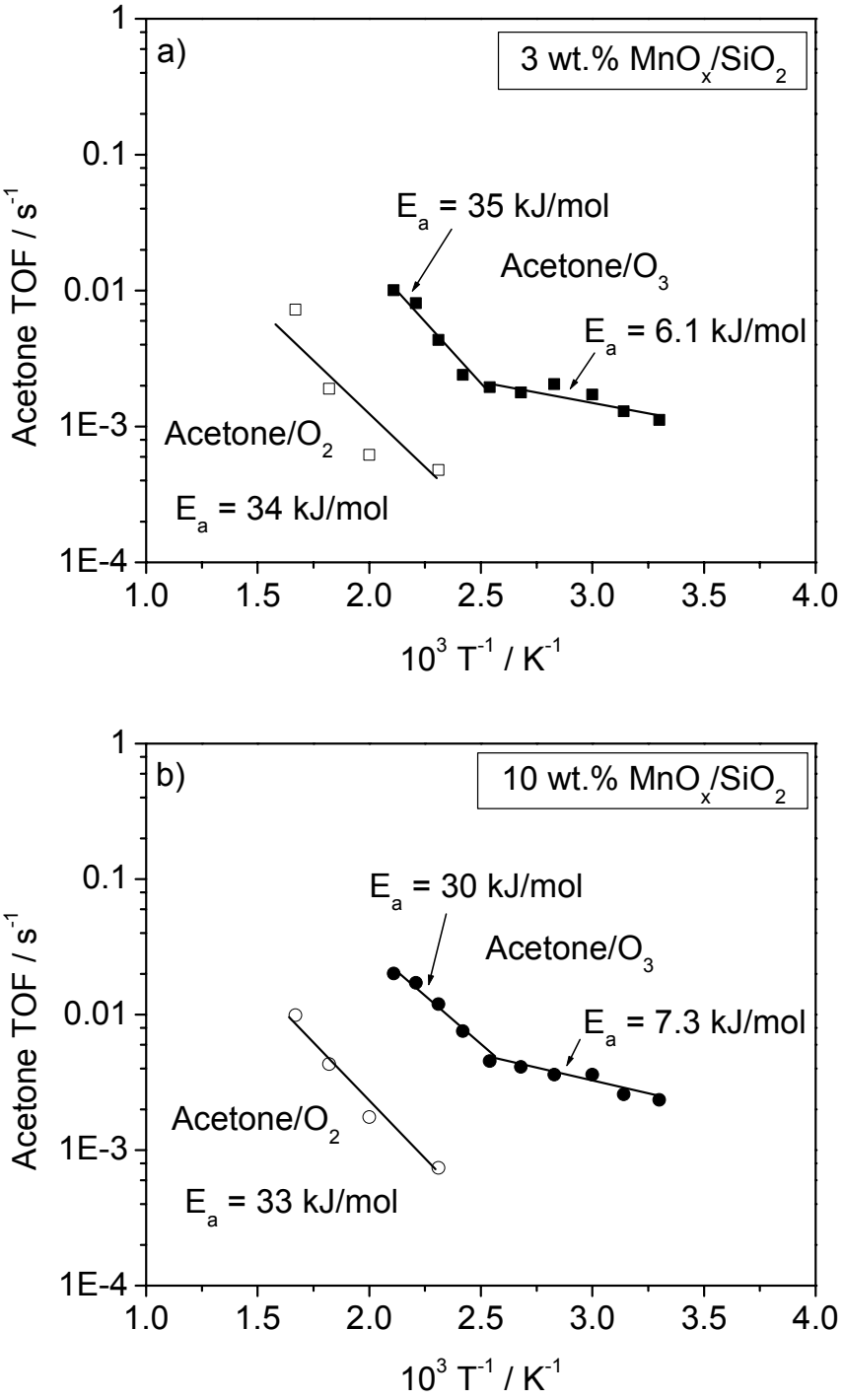

Figure 2.13. Arrhenius plots for acetone conversion over the a) 3 wt. % MnO_x/SiO_2 catalyst and b) the 10 wt. % MnO_x/SiO_2 catalyst for reactions with and without ozone (0.2 mol % acetone, 1 mol % O_3, 34 mol % O_2, 64.8 mol % He).

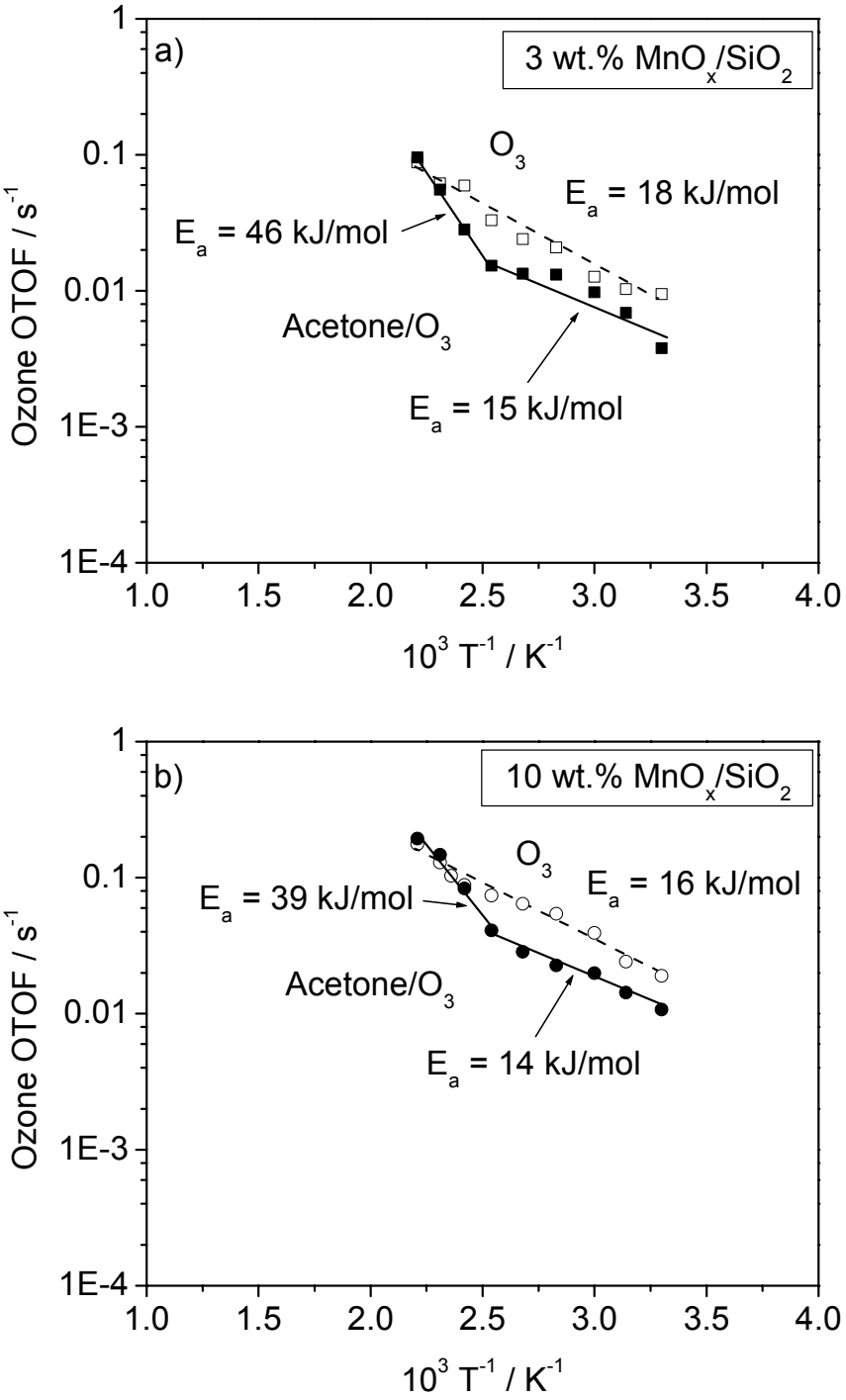

Figure 2.14. Arrhenius plots for ozone conversion over the a) 3 wt. % MnO_x/SiO_2 catalyst and b) the 10 wt. % MnO_x/SiO_2 catalyst for reactions with and without acetone (0.2 mol % acetone, 1 mol % O_3, 34 mol % O_2, 64.8 mol % He).

Much information is presented in Figure 2.13, and for both the 3 and 10 wt. % MnO_x/SiO_2 catalysts, the trends are the same. When ozone was included in the reacting gas mixture, a lower activation energy for acetone conversion was found in the lower temperature region compared to the higher temperature region. In this lower temperature region, the reaction took place on the catalyst surface leading to a decrease in activation energy. The addition of ozone opened a new reaction pathway that resulted in increased catalytic activity at lower temperatures. When ozone was decomposed thermally in the higher temperature region, the reaction became homogeneous, and the activation energy increased. Similarly, there is important information to be gained from Figure 2.14. When comparing activation energies for the 3 wt. % catalyst to the 10 wt. % catalyst, the activation energies for the 10 wt. % catalyst were slightly lower in all cases again confirming it was the most active for ozone conversion.

The TOFs for the ozone utilization were approximately 10 times larger than those for the acetone reaction, and this suggests the following stoichiometry of reaction,

$$CH_3COCH_3 + 8O_3 \longrightarrow 3CO_2 + 3H_2O + 8O_2. \quad (2.3)$$

As can be seen, each ozone molecule produces an oxygen molecule and contributes only one oxygen atom equivalent. Details of the mechanism of reaction and the kinetics are covered in the next chapter. It is clear, however, that the reaction involves a multi-step sequence of elementary steps. The likely steps are listed below.

$$O_3 + * \longrightarrow O_2 + O* \quad (2.4)$$

$$O_3 + O* \longrightarrow O_2 + O_2* \quad (2.5)$$

$$O_2* \longrightarrow O_2 + * \quad (2.6)$$

$$A + \square \rightleftharpoons A\square \quad (2.7)$$

$$A\square + * \rightleftharpoons A* + \square \quad (2.8)$$

$$A* + nO* \longrightarrow \text{products} \quad (2.9)$$

where * represents a surface manganese site, □ represents a silica site, and A represents acetone (CH_3COCH_3). It is beyond the scope of this chapter to explain the detailed evidence for this sequence, as this is covered in the following chapter. However, it should be noted that acetone and ozone adsorb competitively on one type of site, and that a single Mn atom can accommodate the mechanism.

2.3.4 Laser Raman Spectroscopy

Steady-state, *in situ* Raman spectroscopy experiments were performed on the 10 wt. % MnO_x/SiO_2 catalyst under various reaction conditions (Fig. 2.15). The measurements were successful in characterizing the active phase on the catalyst and identifying two adsorbates on the catalyst surface derived from ozone and acetone. This sample was chosen because it had a high enough loading to give a significant signal for the adsorbates while maintaining high dispersion. Figure 2.15a) shows the spectrum of a clean catalyst surface with only oxygen (35 mol %) and helium flowing over the sample, where the broad peak in the range of 640 – 650 cm^{-1} was due to a Mn-O mode [15]. The identification of the exact phase for this catalyst using Raman spectroscopy is difficult due to the similarity in the Raman modes for the various manganese oxide phases in that range. One study summarized the findings of many Raman studies on bulk manganese oxides and reported that β-MnO_2, β-Mn_2O_3 and Mn_3O_4 all have frequencies reported in the 640-650 cm^{-1} range [16]. The same study identified the Raman peak located at ~650

cm^{-1} as characteristic of Mn_3O_4, the most Raman active phase of all manganese oxides. The study concluded that the Raman modes found in this range for the MnO_2 and Mn_2O_3 samples could actually be attributed to Mn_3O_4 formed due to the local heating of the samples during spectrum acquisition. Assuming that there was no local heating due to sample rotation in our experiments, Raman spectroscopy provided further evidence that the most active phase in our catalysts was similar to Mn_3O_4.

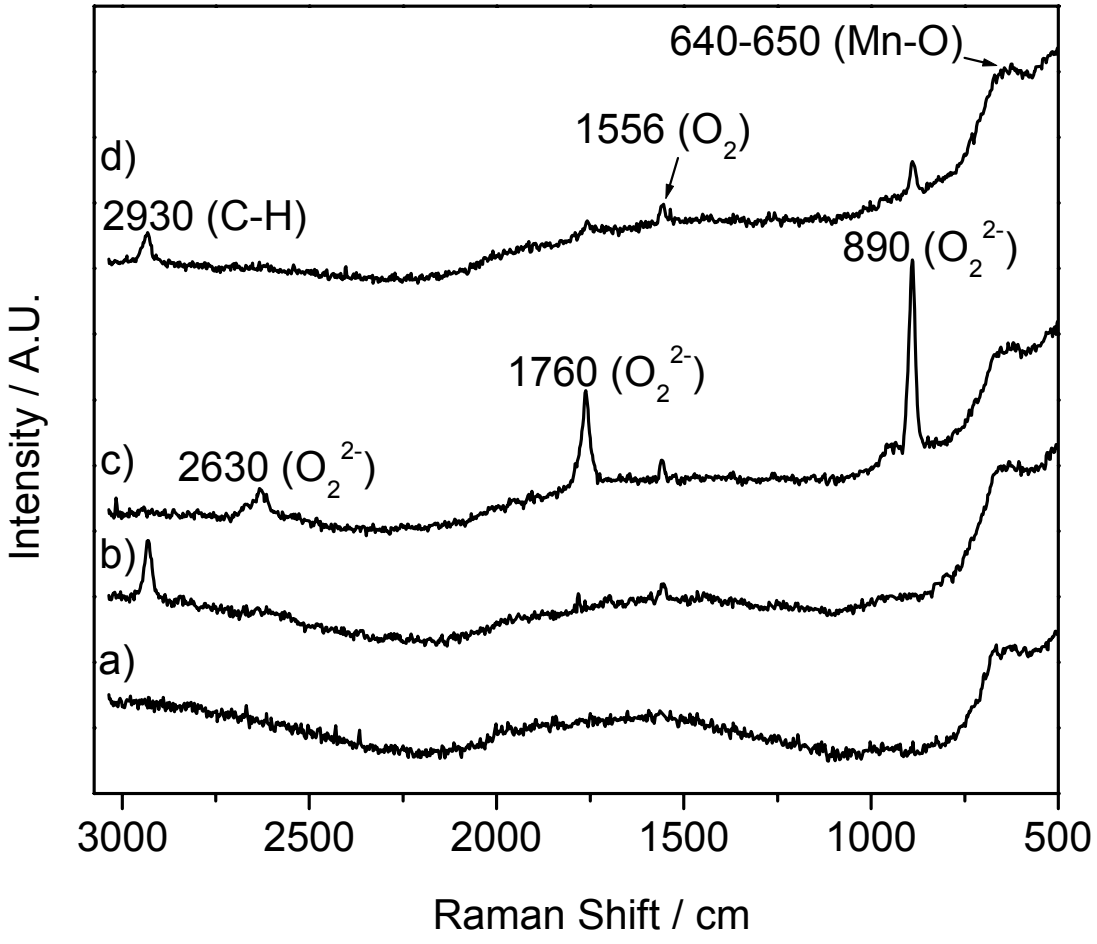

Figure 2.15. Raman spectra of the 10 wt. % MnO_x/SiO_2 exposed to different gas mixtures: a) O_2/He (35 mol % / 65 mol %), b) acetone/O_2/He (0.2 mol % / 35 mol % /

64.8 mol %), c) O_3/O_2/He (1 mol % / 34 mol % / 65 mol %), d) acetone/O_3/O_2/He (0.2 mol %, 1 mol %, 34 mol %, 64.8 mol %).

Figure 2.15b) displays the spectrum of the catalyst when acetone was included in the gas mixture (0.2 mol % acetone, 35 mol % O_2). The presence of acetone resulted in a peak at 2930 cm^{-1} (C-H mode) that can be attributed to an adsorbed acetone species. The CH3 symmetric stretching mode for gas-phase acetone appears at ~2937 cm^{-1} [17]. Also shown in this particular spectrum is a small peak at 1556 cm^{-1}, which is due to gas-phase oxygen. Since the focal point of the collection lens was at the laser spot on the surface of the catalyst sample, the intensity of peaks due to gas-phase species was expected to be weak. This is confirmed by the small signal for the gas-phase oxygen, which is actually in great excess (~4000 %). Figure 2.15c) shows the spectrum of the catalyst surface when only ozone was added to the initial oxygen/helium mixture (1 mol % O_3, 34 mol % O_2). The large peak at 890 cm^{-1} originated from ozone and was identified in previous work done in our laboratory to be due to a peroxide species (O-O band) [18,19]. The features located at 1760 cm^{-1} and 2630 cm^{-1} were overtone bands of the 890 cm^{-1} peak. Figure 2.15d) shows the spectrum of the catalyst surface under reaction conditions when both acetone and ozone were introduced to the sample simultaneously (0.2 mol % acetone, 1 mol % O_3, 34 mol % O_2). In this case, when there was competition for active catalyst sites, the intensity of the peroxide peak due to ozone was significantly diminished whereas the intensity of the peak due to acetone was hardly affected. The measurements indicate that distinct adsorbate peaks for both of the reactants can be observed simultaneously during the course of the reaction.

Figure 2.16 shows the effect of temperature on the acetone adsorption signal at steady-state without the addition of ozone in the feed stream. As shown, the intensity of the adsorbed acetone peak at 2930 cm^{-1} decreased with increasing temperature. Figure 2.17 shows the effect of temperature when both acetone and ozone were included in the feed stream. Again, there was a decrease in the intensity of the adsorbed acetone peak with increasing temperature, but the same trend was not seen for the adsorbed ozone peak at 890 cm^{-1}. The adsorbed ozone peak increased slightly with increasing temperature. These results show that the peroxide species due to ozone was more strongly adsorbed on the catalyst surface than the acetone species. As the temperature was increased, less acetone was adsorbed which freed up sites for ozone adsorption.

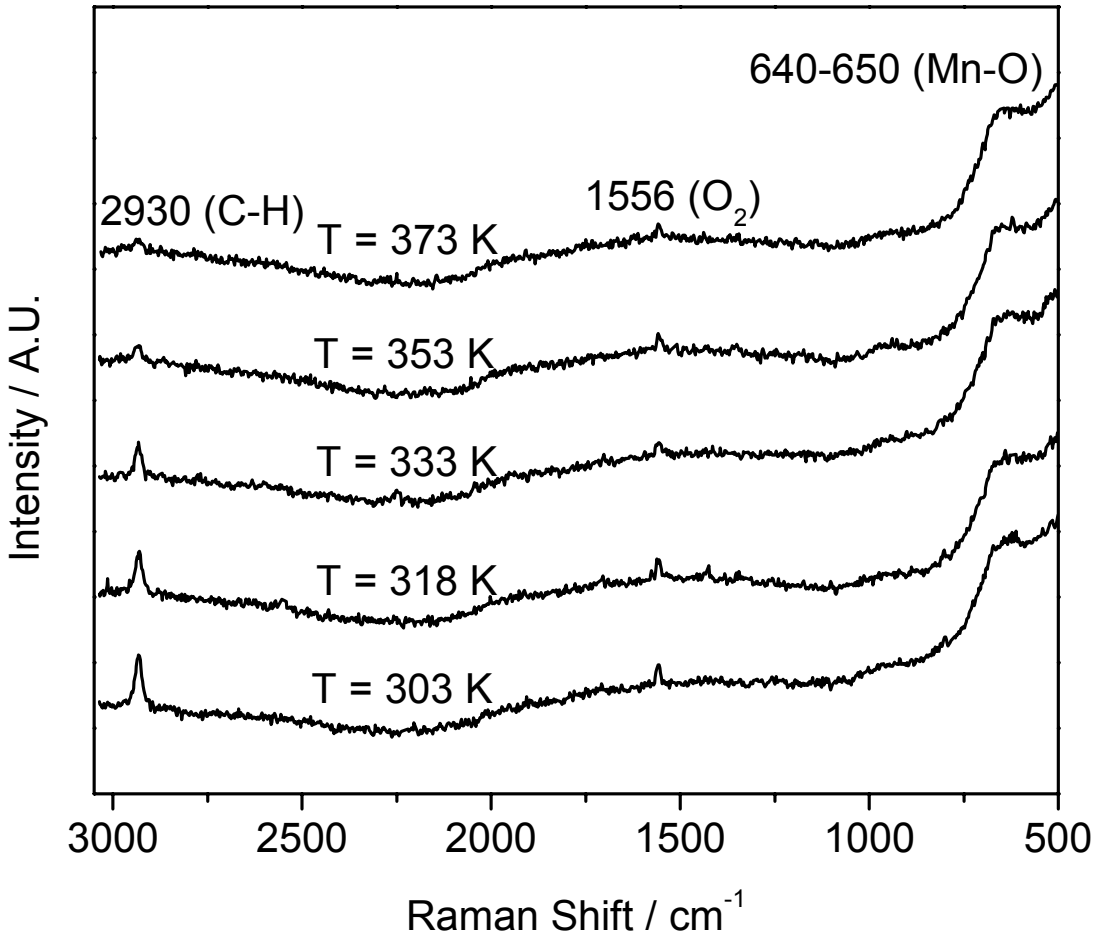

Figure 2.16. Effect of temperature on the Raman spectra for the 10 wt. % MnO_x/SiO_2 catalyst in acetone/O_2/He (0.2 mol % / 35 mol % / 64.8 mol %) flow.

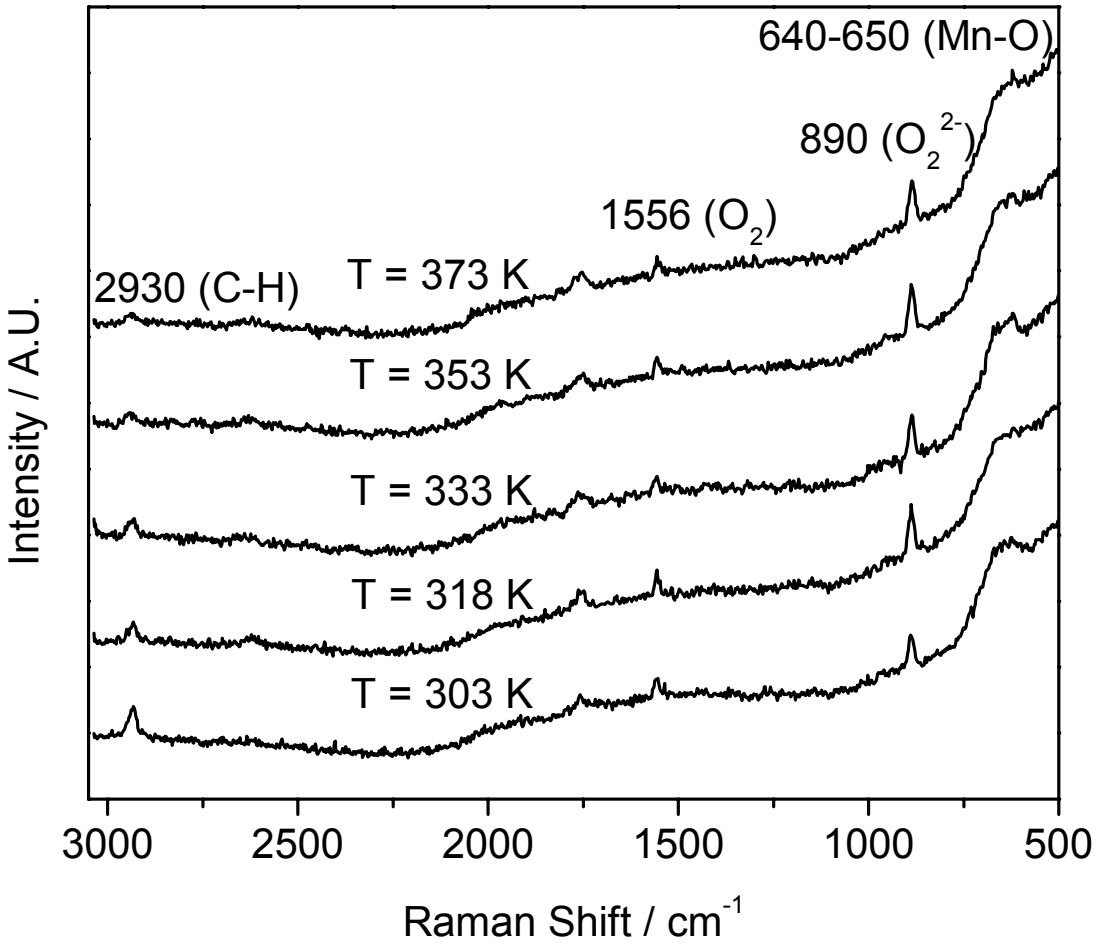

Figure 2.17. Effect of temperature on the Raman spectra for the 10 wt. % MnO_x/SiO_2 catalyst in acetone/O_3/O_2/He (0.2 mol % / 1 mol % / 34 mol % / 64.8 mol %) flow.

2.4 Relationship Between Structure and Reactivity

An important objective of this study is to relate the structure of the catalysts to their reactivity. To review, the EXAFS analysis of the 3 wt. % MnO_x/SiO_2 sample showed that the coordination around each Mn atom was composed of 6 Mn-O distances and no appreciable Mn-Mn contribution, indicating that the Mn clusters were essentially atomically dispersed and had an octahedral structure as shown in Fig. 2.9a). The XANES

spectra suggested an oxidation state close to Mn_2O_3 (+3). The EXAFS analysis of the 10 wt. % MnO_x/SiO_2 sample indicated that it had Mn-O and Mn-Mn distances consistent with a structural unit in Mn_3O_4 as depicted in Fig. 2.9b). The XANES spectra also suggested an oxidation state close to Mn_3O_4 (+2⅔). The white line analysis of the XANES data supported the trend that the Mn oxidation state decreased with increased loading. Thus, the 3 wt. % MnO_x/SiO_2 sample had the Mn in a more dispersed state, with high coordination and a relatively high oxidation state while the 10 wt. % MnO_x/SiO_2 sample had multi-centered Mn oxide clusters with lower Mn coordination and a lower oxidation state. It should be noted that these structures represent the resting state of the catalysts prior to the introduction of the reactants.

The reactivity studies showed that the 3 wt. % MnO_x/SiO_2 sample had lower activity than the 10 wt. % MnO_x/SiO_2 sample for both the acetone/ozone reaction and the ozone decomposition reaction. The reason for the lower reactivity of the lower loading catalyst can be inferred from its structure. As discussed previously, the acetone oxidation reaction is a multi-step reaction. The isolated Mn centers are required to coordinate both acetone and an oxygen species derived from ozone and allow reaction between them. Manganese is an element in the periodic table that is uniquely suited for this because it is capable of high coordination (up to 8 in $[Mn(12C4)_2][MnBr_4]_2[N(CH_3)_4]_2$ [20]) (12C4 = 12-crown-4) and multiple oxidation states (+2, +3, +4, +5, +6, +7 [21]). Clearly, the oxygen equivalents necessary for the oxidation of acetone must come through numerous sequential adsorption steps, possibly as shown in the first reaction in the sequence proposed. It is reasonable to speculate that in a cluster, where several Mn centers are situated in close proximity, the reaction would be facilitated by the easier delivery of

oxygen equivalents and greater ability to accommodate intermediate acetone fragments derived from reaction. This would account for the higher activity of the higher loading sample. The acetone oxidation reaction is a structure-sensitive reaction and is facilitated by multiple adjacent sites.

The lower oxidation state of the higher loading samples also plays a role in its enhanced activity compared to the lower loading samples. It is assumed here that very high oxidation states of Mn are less favored than intermediate states. Since the oxidation state of the clusters in the higher loading samples is lower, they can interact with ozone more readily to form the oxygen species on the catalyst surface. In essence, the rate-determining step is the oxidation of the catalyst by ozone, not the oxidation of the substrate by the catalyst. This is further supported by the positive order of the reaction for ozone discussed in the upcoming chapter.

Overall, the higher activity of the larger clusters in the 10 wt. % MnO_x/SiO_2 sample compared to the isolated Mn clusters in the 3 wt. % MnO_x/SiO_2 can be explained by structural factors related to the transfer of multiple oxygen atoms to the acetone molecule and electronic factors related to the activation of ozone.

2.5 Conclusions

Silica-supported manganese oxide catalysts with loadings of 3, 10, 15, and 20 wt. % (as MnO_2) were characterized using x-ray absorption spectroscopy and x-ray diffraction (XRD). The edge positions in the x-ray absorption spectra indicated that the oxidation state for the manganese decreased with increasing metal oxide loading from a

value close to that of Mn_2O_3 (+3) to a value approximating that of Mn_3O_4 (+2⅔). The XRD was consistent with these results as the diffractograms for the supported catalysts of higher manganese oxide loading matched those of a Mn_3O_4 reference. The reactivity of the silica-supported manganese oxide catalysts in acetone oxidation using ozone as an oxidant was studied over the temperature range of 300 to 600 K. Both oxygen and ozone produced mainly CO_2 as the product of oxidation, but in the case of ozone the reaction temperature and activation energy were significantly reduced. The effect of metal oxide loading was investigated, and the activity for acetone oxidation was greater for a 10 wt. % MnO_x/SiO_2 catalyst sample compared to a 3 wt. % MnO_x/SiO_2 sample. Steady-state, *in situ* Raman spectroscopy experiments were used to investigate the catalyst surface, and two vibrational bands associated with adsorbed intermediates were successfully identified. A band located at 2930 cm^{-1} (C-H mode) was due to adsorbed acetone while a band at 890 cm^{-1} (O-O band) was attributed to a peroxide species originating from ozone.

References

1 A. N. Desikan, L. Huang, S. T. Oyama, Oxygen chemisorption and laser Raman spectroscopy of unsupported and silica-supported molybdenum oxide, *J. Phys. Chem*., **1991**, 95, 10050.

2 A. L. Ankudinov, B. Ravel, J. J. Rehr, and S. D. Congradson, Real-space multiple-scattering calculation and interpretation of x-ray-absorption near-edge structure, *Phys. Rev.B*, **1998**, 58, 7565.

3 R. M. Felder, R. W. Rousseau, "Elementary Principles of Chemical Processes, Second Ed.," John Wiley & Sons: New York, 1986, 235.

4 C. J. Brinker, "Sol-Gel Science: The Physics and Chemistry of Sol-Gel Processing," Academic Press, Inc.: Boston, 1990, 557.

5 M. Seman, J. N. Kondo, K. Domen, R. Radhakrishnan, S. T. Oyama, Reactive and inert surface species observed during methanol oxidation over silica-supported molybdenum oxide, *J. Phys. Chem. B*., **200**2, 106, 12965.

6 M. Boudart, Turnover rates in heterogeneous catalysis, *Chem. Rev*., **1995**, 95, 661.

7 A. N. Desikan, L. Hugang, S. T. Oyama, Oxygen chemisorption and laser Raman specstroscopy of unsupported and silica-supported molybdenum oxide, *J. Phys. Chem.*, **1991**, 95, 10050.

8 X. Wang, P. Clark, S. T. Oyama, Synthesis, characterization, and hydrodreating activity of several iron group transition metal phosphides, *J. of Catal.*, **2002**, 208, 321.

9 V. Baron, J. Gutzmer, H. Rundlof, R. Tellgren, The influence of iron substitution on the magnetic properties of hausmannite, $Mn(Fe,Mn)_2O_4$, *Am. Mineral.*, **1998**, 83, 786.

10 R. W. G. Wyckoff, "Crystal Structures, Vol 2," John Wiley & Sons: New York, 1964, 2.

11 R. W. G. Wyckoff, "Crystal Structures, Vol 1," John Wiley & Sons: New York, 1963, 251.

12 N. M. D. Brown, J. B. McMonagle, An absorption edge and extended x-ray absorption fine structure study of dispersed manganese dioxide oxidation catalyst, *J. Chem. Soc., Faraday Trans. 1*, **1984**, 80, 589.

13 J. M. Thomas, W. J. Thomas, "Principles and Practice of Heterogeneous Catalysis," VCH: Weinheim, 1997, 196.

14 S. T. Oyama, W. Li, W. Zhang, in: H. Hattori, K. Otsuka (Eds.), A comparative study of ethanol oxidation with ozone on supported molybdenum and manganese oxide catalysts, "Science and Technology in Catalysis 1998," (Studies in Surface Science and Catalysis, Vol. 121), Elsevier: Tokyo, 1999, 105.

15 F. Kapteijn, A. D. van Langeveld, J. A. Moulijn, A. Andreini, M. A. Vuurman, A. M. Turek, J. M. Jehng, I. E. Wachs, Alumina-supported manganese oxide catalysts. I. Characterization; effect of precursor and loading, *J. Catal*., **1994**, 150, 94.

16 F. Buciuman, F. Patcas, R. Craciun, D. R. T. Zahn, Vibrational spectroscopy of bulk and supported manganese oxides, *Phys. Chem. Chem. Phys.*, **1999**, 1, 185.

17 NIST Chemistry WebBook, "http://webbook.nist.gov/ " 6, April, 2005.

18 W. Li, S. T. Oyama, Mechanism of ozone decomposition on a manganese oxide catalyst. 1. In situ Raman spectroscopy and ab initio molecular orbital calculations, *J. Am. Chem. Soc*., **1998**, 120, 9041.

19 W. Li, S. T. Oyama, Mechanism of ozone decomposition on a manganese oxide catalyst. 2. Steady-state and transient kinetic studies, *J. Am. Chem. Soc*., **1998**, 120, 9047.

20 H. O. N. Reid, I. A. Kahwa, "Intense photosensitized emission from stoichiometric compounds featuring Mn^{2+} in seven- and eightfold coordination environments," *Inorg. Chem*. **1998**, 37, 3868.

21 F. A. Cotton, G. Wilkinson, "Advanced Inorganic Chemistry, 4^{th} Ed.," John Wiley & Sons, Inc.: New York, 1980.